Received: Added at production | Revised: Added at production | Accepted: Added at production

DOI: xxx/xxxx

RESEARCH ARTICLE

Synthetic turbulence modelling for offshore wind farm engineering models using coherence aggregation

Valentin Chabaud

[1]SINTEF Energy Research, Norway

Correspondence

Valentin Chabaud
SINTEF Energy Research, NO-7465,
Trondheim, Norway
Email: valentin.chabaud@sintef.no

Abstract

Turbulent wind fields are known to be a major driver for structural loads on offshore wind turbines, and hence benefit from well-established design standards using wind spectra and coherence functions calibrated from years of measurements. Multiple 10-minutes wind field realisations obtained by Gaussian process generation are then used in aero-hydro-servo elastic codes to get structural loads. When it comes to large offshore wind farms, however, measurements reveal the importance of large, low-frequency turbulent vortices —previously overlooked in the so-called "spectral gap"— for power fluctuations and hence for wind farm control and grid integration. Also, farm-scale wind fields are needed as input to farm-scale aero-servo-elastic codes for the modelling of wake dynamics. These new concerns motivate an upgrade in the original turbine-scale wind field representation: (1) spectral models need to be based on farm-scale measurements, (2) the frozen-turbulence assumption merging temporal and along-wind coherence must be lifted, (3) simplifications are needed to reduce the number of degrees of freedom as the domain becomes excessively large. This paper suggests models and algorithms for *aggregated* synthetic turbulence generation —lumping the wind field into space-averaged quantities— adapted to the aero-hydro-servo elastic modelling of large wind farms. Starting from the work of Sørensen et al. in the early 2000s for grid integration purposes, methods for load modelling (through wake meandering and high-resolution wind field reconstruction) are introduced. Implementation and efficiency matters involving mathematical subtelties are then presented. Finally, numerical experiments are carried out to (1) verify the approach and implementation against a state-of-the-art point-based —as opposite to aggregated— synthetic turbulence generation code, and (2) illustrate the benefit of turbulence aggregation for the modelling of large offshore wind farms.

KEYWORDS:

Synthetic turbulence; Wind farm simulations; Aggregated spectral modelling

1 | INTRODUCTION

Offshore wind energy technology becoming more and more mature, plant size has evolved from arrays of a handful of turbines to 50, 100 turbines and more for newly installed and planned farms. To further reduce costs and make the technology truly competitive, integrated system-level modelling is identified as a major challenge [1]. However, while engineering aero-hydro-servo elastic (AHSE) models have been successfully developed at the turbine level, the farm level presents challenges that have not yet been satisfactorily addressed. One of these challenges is linked to

atmospheric modelling, which is another major challenge [1]. While high-fidelity Large Eddy Simulation (LES) solvers are available, their exceeding computational cost does not qualify them as engineering models. The current engineering approach as suggested in the IEC standard is to split the modelling of ambient wind on the one side with the disturbed wake flow on the other side, later summed using the superposition principle [2,3].

Leading-edge codes such as DTU's HAWC2 or DNV's Bladed focus on single turbines, precomputing both the ambient and wake flows prior to simulation. In practice, a so-called *turbulence box* is generated whose slices correspond to wind input for each simulation time step. While this sequential approach is efficient for load analysis, it cannot handle feedback effects from turbines to flow that would happen at runtime –e.g. through wind farm control. A notable recent advance has been achieved through the development of NREL's FAST.Farm, where the whole farm is simulated simultaneously with each turbine running its own AHSE model in parallel [4,5]. This gives the possibility to incorporate farm-wide flow dynamics and controls. However, while farm-wide wake flow dynamics are indeed captured, inherent limitations in ambient wind modelling inhibit the practical inclusion of farm-wide turbulence. Extending the traditional methods generating fine-meshed turbulent boxes is an option when considering an array of few turbines [6], but becomes infeasible when looking at a utility scale farm: the computational cost increases cubically with the number of points, becoming excessively large as the box would need to 1) cover the entire farm area instead of one single rotor and 2) be augmented along an additional dimension as variations in time and in space along wind no longer can be interchanged (the so-called Taylor's frozen-turbulence assumption is no longer valid for the large inter-turbine distances, as the turbulence at a downstream points is not simply linked to an upstream point by a time delay). The alternatives are 1) LES-based modelling of ambient flow, and 2) independent generation of turbulent boxes for each turbine [4]. The first option, although cheaper than LES simulations with wind turbines present, is still too impractical to be qualified for mid-fidelity engineering modelling. The second option is inherently wrong for the purpose of this paper to model farm-wide turbulence.

The perhaps most visible consequence of farm-wide turbulence is fluctuations in power production arising from large coherent turbulence patterns across several turbines, if not the entire farm. Toward more accurate models for grid integration purposes, this led Sørensen and Vigueras-Rodriguez's research group to develop simplified wind turbine and farm models using farm-level turbulence modelling [7,8,9,10]. As part of this development, farm-level turbulence was characterised, showing the significance of large, low-frequency turbulent vortices in existing offshore farms [9,10], arising from mesoscale diurnal variations depending on atmospheric stability [11]. Further, noticing that small, high-frequency vortices — although important for loads— do not significantly affect rotor dynamics and hence power output (the large rotor inertia and swept area acting as low-pass filters), the idea of coherence aggregation came out [7,8]. As only rotor-averaged quantities are of interest, the averaging operation is performed beforehand in the frequency domain instead of during simulation in the time domain. This bypasses the need of modelling turbulence on a fine grid only to, in turn, average it out, thus reducing complexity tremendously. However, the simplified farm models for which coherence aggregation has been originally developed are inherently limited. First they are not comprehensive AHSE models able to capture the dynamic response of the turbines, and they do not include disturbed (wake) flow.

This paper presents the theoretical background enabling the adaption of coherence aggregation for practical use in farm-level AHSE simulation softwares (among other applications). The novelty is three-fold. First, the paper addresses specific challenges linked to a major difference with the work of Sørensen: aggregated turbulence needs not only to be modelled at each turbine, but also downstream of turbines where it drives wake meandering (in practice, aggregated turbulence needs to be modelled on a regularly spaced grid discretising the entire farm area). Second, the method is extended to model the turbulent fluctuations of the spatially linearised variations of the wind speed across the turbines' rotor (the so-called horizontal and vertical linear wind shears), correlated with aggregated shears and axial turbulence on other (neighbour) turbines. Third and perhaps most importantly, a method for constrained turbulence with no information loss is suggested, to (1) construct a wind field over the entire farm area knowing the wind field at the turbines and (2) reconstruct a full-field high-resolution wind field at the turbines given an aggregated realisation (i.e. the inverse of aggregation) is given, thus providing a method for generating correlated high-resolution turbulent boxes across the farm.

The paper is organised as follows: The Veers method for frequency-domain synthetic turbulence generation for single turbines is first introduced. It is then progressively extended to farm-wide applications through lifting of the frozen-turbulence assumption, coherence aggregation, inclusion of shear components and full-field reconstruction. Specific challenges linked to the synthetic generation of aggregated quantities between closely spaced points are then addressed. A numerical verification against full-field realisations from state-of-the-art verified code is then performed, and the efficiency of the various concepts and algorithms suggested in the paper is illustrated.

A note on scales

The correlation of atmospheric turbulence decays exponentially with both distance and frequency (see (1)), meaning that low-frequency vortices are large, and high-frequency vortices are small. From the turbine point of view, vortices larger than a couple of times the rotor diameter correspond to a timescale of approximately 10 minutes. They may be seen as quasi-static variations, explaining why 10-min simulations are often used to characterise loads [3,12]. However, from the farm point of view, vortices that cover the entire area of a utility-scale farm (100 turbines) typically have periods of several hours. In between, vortices may be just large enough to influence clusters of turbines but not the entire farm. This results in power fluctuations and changes in the disturbed wake flow, hence driving the wind conditions at the minutes timescale. This separation of

length- and timescales suggests a nested approach, where farm level feeds into turbine level. This paper focuses on the farm level, but also offers the possibility to jointly model the two levels simultaneously through long simulations (typically one hour) capturing farm-wide effects while still featuring high resolution at the turbine scale.

2 | THE VEERS METHOD

Joint random generation of multiple correlated stationary processes from their spectral representation dates back to the work of Shinozuka [13] and has become a standard method used in a variety of applications where multiple stochastic inputs are correlated in space, such as seismic vibrations or wind [14]. Veers [15] adapted it to wind energy, initiating the current approach of precomputing turbulent boxes propagated through the rotor at simulation time under Taylor's frozen-turbulence assumption. The method relies on Cholesky factorisation and random phases to come up with a turbulent box realisation that satisfies spectral properties fitted from field measurements.

Notations and coordinate system

The NWU (North-West-Upward) coordinate system with wind direction pointing northward (standard for AHSE codes) is used. Coordinates/axes are noted $(\mathsf{x}, \mathsf{y}, \mathsf{z})$ and corresponding wind velocity components $(\mathsf{u}, \mathsf{v}, \mathsf{w})$. The slash symbol / used in subscripts switches between components for a more compact notation, not to be confused with the divider operator always represented in fraction format.

2.1 | Spectral representation of turbulence

The spectral properties are first the power spectral density (PSD), that tells how the energy carried by wind velocity at a specific point in space is distributed as function of frequency. The second spectral property is the coherence (actually only its real part), characterising by how much the wind velocities u_1 and u_2 at two specific points in space are correlated with each other:

$$\gamma_{u_1u_2} = \frac{|S_{u_2u_1}|}{\sqrt{S_{u_1u_1}S_{u_2u_2}}} = \gamma_{u_2u_1}\left(\mathbf{p}, f, \vec{r}_{12}\right)$$

With $\mathsf{S}_{\mathsf{u_2u_1}}$ the –in general– complex-valued cross spectral density (CSD), $\mathsf{S}_{\mathsf{u_iu_i}}$ the PSD at point i, $\mathbf{p}$ a set of parameters characterising the wind condition (mean wind speed, direction, atmospheric stability, turbulence intensity...), f the frequency and $\overrightarrow{\mathsf{r}}_{12}$ the position vector from point 1 to 2. This coherence of atmospheric turbulence mathematically defines the spatio-temporally correlated flow patterns known as turbulent *vortices*, while the power spectral density represents their strength.

Engineering AHSE models benefit from well-defined standards providing spectral models to model turbulence at the turbine/minutes scale. At the farm/hours scale, however, turbulence is highly site-dependent and meteorological studies using field measurements and high-fidelity simulations have not led yet to a consensus that may be used to define a standard engineering procedure. At offshore locations —but also on land [16]—, the so-called spectral gap, showing no turbulence for periods 10 minutes to 4 hours with least content at 1 hour, has been widely questioned. Worth mentioning are the works of Larsén at al. [17,18,19], Cheynet et al. [11] and Vigueras-Rodriguez [9,10].

A generic model for the coherence reads

$$\gamma_{u_1u_2}\left(\mathbf{p}, f, \vec{r}_{12}\right) = e^{-\|\mathbf{a}\otimes\vec{r}_{12}\|\sqrt{\left(\frac{f}{u_\infty}\right)^2+\left(\frac{\|\mathbf{b}\otimes\vec{r}_{12}\|}{\|\vec{r}_{12}\|}\right)^2}} \tag{1}$$

where $\mathbf{a}$ is a vector of decay factors for each direction, and $\mathbf{b}$ an offset vector forcing coherence to decrease with distance at zero frequency. Seeking for a farm-wide model maintaining high accuracy at the turbine scale, a starting point may be the model of Vigueras-Rodriguez et al. [10] for the farm-level coherence, viz.

$$\mathbf{a}_{farm} = \begin{bmatrix}\mathsf{a}_{\mathsf{long}} & \mathsf{a}_{\mathsf{lat}} & \mathsf{N/A}\end{bmatrix}^T \;;\; a_{lat} = c_1\frac{u_\infty}{\|\vec{r}_{12}\|} + c_2;\;\; \mathbf{b}_{farm} = \mathbf{0}_{3\times1} \tag{2}$$

where $\mathsf{a}_{\mathsf{long}}$, c_1 and c_2 are empirical coefficients, and $\mathbf{0}$ the zero matrix/vector. For physical consistency and numerical efficiency (see Sec. 4.3.4), the boundary between turbine and farm scales should be continuous and the coherence should be decreasing with distance and frequency. The following suggestion matches these requirements by introducing a transition distance $\mathsf{d}_{\mathsf{b_y}}$ at the boundary while putting more focus on farm-level coherence:

$$\mathbf{a} = \begin{bmatrix}\mathsf{a}_{\mathsf{long}} & \mathsf{a}_{\mathsf{lat}} & \mathbf{a}_{\mathsf{turb_z}}\end{bmatrix}^T \;;\; a_{lat} = \begin{cases}\mathbf{a}_{\mathsf{turb_y}} & \|\tilde{\mathsf{r}}_{12}\| \le \mathsf{d}_{\mathsf{b_y}} \\ \mathsf{c}_1\frac{\mathsf{u}_\infty}{\|\tilde{\mathsf{r}}_{12}\|} + \mathsf{c}_2 & \|\tilde{\mathsf{r}}_{12}\| \ge \mathsf{d}_{\mathsf{b_y}}\end{cases};\; d_{b_y} = \frac{c_1u_\infty}{\mathbf{a}_{turb_y} - c_2};\;\; \mathbf{b} = \mathbf{0}_{3\times1} \tag{3}$$

which removes the offset represented by $\mathbf{b}$, arguing it has become obsolete at it used to model low-frequency effects at the turbine level, now overridden by the farm-level coherence model. The turbine-level decay factors $\mathbf{a}_{\text{turb}}(\mathbf{p})$ is given by standards[3,12] or site-specific models[11,20].

2.2 | Random Gaussian process generation

Extending from two to n points, the symmetric $n \times n$ coherence matrix $\mathbf{\Gamma}$ reads

$$\mathbf{\Gamma} = \begin{bmatrix} 1 & \cdots & \gamma_{u_1 u_n} \\ \vdots & \ddots & \vdots \\ \gamma_{u_n u_1} & \cdots & 1 \end{bmatrix} = \begin{bmatrix} 1 & \cdots & \frac{S_{u_1 u_n}}{S_u} \\ \vdots & \ddots & \vdots \\ \frac{S_{u_n u_1}}{S_u} & \cdots & 1 \end{bmatrix}$$

Where it has been assumed that the process is ergodic, meaning the power spectral density S_u is the same for all points (this assumption is not necessary, but will be used throughout the paper for the sake of simplicity). The cross spectral matrix $\mathbf{S}$ relates to the Fourier transform $\mathbf{U}$ of the wind velocity timeseries we want to generate through the outer product:

$$\mathbf{S}(\mathbf{p}, f) = \mathbf{\Gamma}(\mathbf{p}, f)\ S_u(\mathbf{p}, f) = \mathbf{U}\mathbf{U}^H \tag{4}$$

with ^{H} the Hermitian (transpose and complex conjugate) operator. The goal is then to find a realisation of $\mathbf{U}(\mathbf{p}, f)$ that satisfies (4), for each frequency for a given wind condition. The timeseries are then obtained from inverse Fourier transform. Writing element j of $\mathbf{U}$ in complex modulus and argument form $\mathbf{U}_j = |\mathbf{U}_j| e^{i\angle \mathbf{U}_j}$, it appears that while $|\mathbf{U}_j| = \sqrt{S_u}$ is trivial, solving for the complex argument involves an overdetermined system of $\frac{n(n-1)}{2}$ equations with full rank for n unknowns. There is therefore no deterministic solution to (4), but it can be solved in the stochastic sense using the average $\langle \mathbf{U}\mathbf{U}^H \rangle$ over frequencies and realisations (i.e. simulations) instead of $\mathbf{U}\mathbf{U}^H$:

$$\left\langle \mathbf{U}\mathbf{U}^H \right\rangle = \mathbf{\Gamma} S_u \tag{5}$$

If $\mathbf{\Gamma}$ can be expressed as a product of matrix square roots $\mathbf{\Gamma} = \mathbf{A}\mathbf{A}^H$, a solution to (5) is

$$\mathbf{U} = \sqrt{S_u}\, \mathbf{A}\, \mathbf{\Phi} \tag{6}$$

where $\mathbf{\Phi} = \left[e^{i\phi_1} \cdots e^{i\phi_n} \right]^T$ is a phase angle vector, the phases ϕ_i being random and independent such that $\langle \mathbf{\Phi}\mathbf{\Phi}^H \rangle = \mathbf{I}_n$ the identity matrix. A particular square root of $\mathbf{\Gamma}$ that is convenient to use is the lower-triangular Cholesky factor $\mathbf{L}$, obtained by Cholesky factorisation. The complete set of solutions may be obtained by multiplication of $\mathbf{L}$ with the space of orthogonal matrices.

2.3 | Taylor's frozen-turbulence assumption

Conceptualising the turbulence input as a three-dimensional "box" is made possible thanks to the confusion between space and time. Time variations and along-wind spatial variations advected with the mean wind speed are assumed equivalent. This is known as Taylor's frozen-turbulence assumption (or hypothesis) and is a pillar of the Mann model for synthetic turbulence generation where wave numbers (spatial variations) are used instead of frequencies (time variations)[21]. For the Veers model, this assumption is not necessary *in theory*, but in practice not making it would require one 3D turbulence box per time step (or conceptually a 4D box) covering all along-wind locations where wind will/could be evaluated. For single turbines, modelling at multiple along-wind locations is only needed to encompass the unknown yet small turbine motions, so the frozen-turbulence assumption is reasonable. For farms however, it would be equivalent to assuming that downstream turbines experience the same ambient wind fluctuations as upstream turbines, simply delayed by the advection time. This is obviously oversimplifying, as vortices undergo changes along the way.

Mathematically, this time delay is described by the imaginary part of the coherence between two points as function of along-wind distance. The coherence becomes complex-valued, and its argument reads

$$\angle \mathbf{\Gamma}_{ij} = \mathbf{\Theta}_{ij} = e^{-2\pi f \frac{\vec{e}_x^T \vec{r}_{ij}}{\overline{\overline{u}}_{ij}}} \tag{7}$$

with $\tilde{e}_x$ the unitary vector in along-wind direction and $\overline{\overline{u}}_{ij}$ the equivalent advection wind speed between points i and j. This makes the random process generation method described in 2.2 more complicated. While Sørensen suggested an ad-hoc method[8], further simplification is possible by realising that if $\overline{\overline{u}}_{ij}$ is constant, the phase angle matrix $\mathbf{\Theta}$ might be directly transferred to the coherence matrix and its square root[14], viz.

$$\mathbf{L} = \mathbf{L} \odot \mathbf{\Theta};\quad |\mathbf{\Gamma}| = \mathbf{L}\mathbf{L}^T;\quad \mathbf{\Gamma} = |\mathbf{\Gamma}| \odot \mathbf{\Theta} \tag{8}$$

with $|\mathbf{\Gamma}|$ the modulus of the now complex $\mathbf{\Gamma}$ and $\odot$ the Hadamard (elementwise) product. The solution (6) may then simply be updated to

$$\mathbf{U} = \sqrt{S_u}\ (\mathbf{L} \odot \mathbf{\Theta})\ \mathbf{\Phi} \tag{9}$$

Although it will be affected by non-stationary changes (e.g. from wake flow control), assuming $\overline{\overline{\mathrm{u}}}_{\mathrm{ij}}$ as constant is deemed consistent with the current mid-fidelity approach. A model for $\overline{\overline{\mathrm{u}}}_{\mathrm{ij}}$ is given by Vigueras-Rodriguez based on data from large Danish offshore wind farms as

$$\overline{\overline{u}}_{ij} = \kappa u_\infty \tag{10}$$

with u_∞ the undisturbed mean wind speed and κ a constant fitted to $\kappa \approx 0.85$ [10], which may be interpreted as an approximate inclusion of wake velocity deficit and atmospheric boundary layer/blockage effects.

3 | COHERENCE AGGREGATION

As a result of Sec. 2.3, the modulus and argument of the complex coherence matrix may be dissociated. In the following, coherence refers only to the modulus part, the argument being characterised by (7) and (10).

3.1 | Spatial averaging

As mentioned in Sec. 2.3, a 4D turbulence box solving (9) for the entire farm at each time step would be needed. The Cholesky factorisation having a computational cost of $\mathcal{O}\left(\mathrm{n}^3\right)$, this approach would quickly prove infeasible if point-based velocities were to be calculated with the same resolution as for single turbines. Since space-averaged values are sufficient for the purpose of farm-level flow modelling, turbulence may be lumped at the centre of control domains representing elements discretising the farm domain with a much coarser resolution than if point-based values were used[1]. Noting Ω_i the control domain of element i, $\bar{\mathrm{u}}_\Omega$ the time-domain average of u over the element, and $\mathcal{F}\{\,\}$ the Fourier transform operator, the weighted aggregated coherence $\overline{\gamma}_{\Omega_{u_1 u_2}}$ between two elements is derived by averaging the point-based coherence between all pairs of points, adapting the work of Sørensen [7]:

$$\overline{\gamma}_{\Omega_{u_1 u_2}}\left(\mathbf{p}, f, \vec{r}_{0_1 0_2}\right) = \frac{\int_{\Omega_1}\int_{\Omega_2} \gamma_{u_1 u_2}\left(\mathbf{p}, f, \vec{r}_{12}\right)\ \psi_{\Omega_1}\left(\vec{r}_{0_1 1}\right)\psi_{\Omega_2}\left(\vec{r}_{0_2 2}\right) d\Omega_1 d\Omega_2}{\int_{\Omega_1}\int_{\Omega_2} \psi_{\Omega_1}\left(\vec{r}_{0_1 1}\right)\psi_{\Omega_2}\left(\vec{r}_{0_2 2}\right) d\Omega_1 d\Omega_2} \tag{11}$$

with $\overrightarrow{\mathrm{r}}_{\mathrm{ij}}$ a position vector from i to j, 0_i being the centre of element i, and $\overrightarrow{\mathrm{r}}_{12}$ reading $\overrightarrow{\mathrm{r}}_{12} = \overrightarrow{\mathrm{r}}_{0_1 0_2} + \overrightarrow{\mathrm{r}}_{0_2 2} - \overrightarrow{\mathrm{r}}_{0_1 1}$. ψ_{Ω_i} is a weighting function associated with element i, which can represent

- the wind profile, i.e. variations in wind speed with altitude resulting from ground friction and pressure/temperature gradients[2].
- mapping functions from axial wind speed to other stochastic quantities, such as linear wind shears or aerodynamic loads[3]

The PSD of the aggregated wind speed is obtained by averaging on the same element (i.e. $0_1 = 0_2$):

$$S_{\bar{u}_\Omega}\left(\mathbf{p}, f\right) = \mathcal{F}\left\{\frac{\int_{V_1}\psi_\Omega\left(\vec{r}_{0_1 1}\right) u\left(\mathbf{p}, t, \vec{r}_{0_1 1}\right) dV_1}{\int_{V_1}\psi_\Omega\left(\vec{r}_{0_1 1}\right) dV_1}\right\}^2 = \overline{\gamma}_{\Omega_{u_1 u_2}}\left(\mathbf{p}, f, 0\right) S_u\left(\mathbf{p}, f\right) = \left|G_{\Omega_u}\left(\mathbf{p}, f\right)\right|^2 S_u\left(\mathbf{p}, f\right) \tag{12}$$

where $\mathrm{G}_{\Omega_\mathrm{u}}$ is the resulting transfer function, called the *admittance* function. The coherence between aggregated quantities $\gamma_{\bar{\mathrm{u}}_{\Omega_1}\bar{\mathrm{u}}_{\Omega_2}}$ may then be derived from the aggregated coherence between point-based quantities $\overline{\gamma}_{\Omega_{u_1 u_2}}$ as

$$\gamma_{\overline{u}_{\Omega_1}\overline{u}_{\Omega_2}}\left(\mathbf{p}, f, \vec{r}_{0_1 0_2}\right) = \frac{\overline{\gamma}_{\Omega_{u_1 u_2}}\left(\mathbf{p}, f, \vec{r}_{0_1 0_2}\right)}{\left|G_{\Omega_{u1}}\left(\mathbf{p}, f\right)\right|\left|G_{\Omega_{u2}}\left(\mathbf{p}, f\right)\right|} \tag{13}$$

where $\mathrm{G}_{\Omega_{u_1}}$ and $\mathrm{G}_{\Omega_{u_2}}$ are kept distinct on purpose as they may use distinct weighting functions.

The choice of the integral domain Ω depends on whether we work with *cell-averaged* or *rotor-averaged* quantities. Rotor averaging is appropriate to model load-equivalent wind speeds[3] and is performed over a disk of the size of the rotor. Wake dynamics as modelled in the Dynamic Wake

[1] Current practice using point-based representations at coarse resolutions is an oversimplification, made for convenience while overlooking induced errors

[2] The wind profile is not directly taken into account in standard wind spectra (Kaimal, Von Karman) which are defined as uniform. However, scaling of wind speed according to wind profile (including turbulent fluctuations) is typically done later on when used in wind turbine simulators.

[3] The weighting function for rotor averaging may incorporate the radial distribution of thrust/power coefficients along the blade, giving thrust and power-equivalent wind speeds. In practice, however, it appears that unitary radial weighting is sufficient to map wind speed to aeroydnamic loads, hence no distinction between thrust and power is necessary, nor between cell- and rotor-averaging, as far as the weighting function is concerned.

Meandering model are also driven by disc-averaged fluctuations, but an additional filter is used to remove the effect of small vortices [2]. Improvements of the model in FAST.Farm also make use of averaged fluctuations to update the eddy viscosity responsible for wake recovery and crucial in velocity deficit modelling [4]. As we are talking about volumetric quantities, 3D averaging using volume (triple) integrals over cuboid cells may be conceptually more appropriate in this case although this is open to discussion.

Note that the solution given by (16) depends on the choice of integral domain. Simulating both cell-averaged and rotor-averaged quantities would require solving (16) twice while ensuring consistency between the two solutions. This is addressed by using cascaded simulations, presented in Sec. 3.3.1.

In summary, the space-averaged turbulence may be characterised by aggregated spectral quantities given by (12) and (13), involving a sextuple or quadruple integral (each cell integral being triple or double depending on whether we look at cell-averaged or rotor-averaged quantities) of the point-based coherence function. Realisations may then be obtained by the Veers method described in Sec. 2.

3.2 | Linear shear components

The term *quantities* has been used on purpose, as not only the axial wind speed u can be modelled using Veers method and coherence aggregation. Spatial variations may be characterised by playing with the weighting function. This way, the linear shear components $\mathsf{s_y}$ and $\mathsf{s_z}$ (respectively vertical and horizontal) may be added, representing fluctuating linear speed variations on top of the mean wind profile. Although not directly used in engineering wake models, shears may be used in inter-turbine ambient flow modelling for turbulence intensity estimations based on spatial averaging. They are however more important at the turbines, where augmenting the rotor-based load-equivalent wind speed vector with shears is valuable to capture blade loads by rotational sampling of non-uniform wind field as well as tangential rotor loads (particularly yaw and pitch moments), especially on floating offshore wind turbines [22]. It may readily be included in actuator-disc (hub-height) wind input models in OpenFAST [5] and used in advanced actuator disc models [23].

Taking the vertical shear $\mathsf{s_y}$ as an example and noting $\mathsf{z} = \mathsf{e_z^T}\tilde{\mathsf{r}}_{0_1 1}$, we are looking for equivalent linear vertical variations yielding

$$\int_{\Omega_1} s_y z^2 d\Omega_1 = \int_{\Omega_1} u\left(\mathbf{p}, t, \vec{r}_{0_1 1}\right)\, z\, d\Omega_1 \tag{14}$$

Therefore, the aggregated transfer functions, PSD and spectra for $\mathsf{s_y}$ and $\mathsf{s_z}$ may be obtained using (11), (12) and (13) with respectively $\psi = \mathsf{e_z^T}\tilde{\mathsf{r}}_{0_\mathsf{i}\mathsf{i}}$ and $\psi = -\mathsf{e_y^T}\tilde{\mathsf{r}}_{0_\mathsf{i}\mathsf{i}}$ in the numerator, and their squared value in the denominator:

$$\overline{\gamma}_{s_{y_2} s_{y_1}}\left(\mathbf{p}, f, \vec{r}_{0_1 0_2}\right) = \frac{\int_{\Omega_1}\int_{\Omega_2} \gamma_{u_2 u_1}\left(\mathbf{p}, f, \vec{r}_{12}\right)\, e_z^T \vec{r}_{0_1 1}\, e_z^T \vec{r}_{0_2 2}\, d\Omega_1 d\Omega_2}{\int_{\Omega_1}\int_{\Omega_2} \left(e_z^T \vec{r}_{0_1 1}\right)^2 \left(e_z^T \vec{r}_{0_2 2}\right)^2 d\Omega_1 d\Omega_2}; \quad \left|G_{\Omega_{s_y}}\left(\mathbf{p}, f\right)\right|^2 = \overline{\gamma}_{s_{y_2} s_{y_1}}\left(\mathbf{p}, f, 0\right)$$

and likewise for $\mathsf{s_z}$ and rotor-based quantities.

The aggregated coherence as in (13) may also be defined between the mean axial turbulence u (thereafter referred to as fundamental component) and shear components, resulting in a $3\mathsf{n} \times 3\mathsf{n}$ coherence matrix $\mathbf{\Gamma}$ reading

$$\mathbf{\Gamma} = \begin{bmatrix} \mathbf{\Gamma}_{\mathsf{uu}} & \mathbf{0}_{\mathsf{n}\times\mathsf{n}} & \mathbf{\Gamma}_{\mathsf{s_z u}} \\ \mathbf{0}_{\mathsf{n}\times\mathsf{n}} & \mathbf{\Gamma}_{\mathsf{s_y s_y}} & \mathbf{0}_{\mathsf{n}\times\mathsf{n}} \\ \mathbf{\Gamma}_{\mathsf{us_z}} & \mathbf{0}_{\mathsf{n}\times\mathsf{n}} & \mathbf{\Gamma}_{\mathsf{s_z s_z}} \end{bmatrix} \tag{15}$$

where cross terms $\mathbf{\Gamma}_{\mathsf{us_y}} = \mathbf{\Gamma}_{\mathsf{s_y u}} = \mathbf{\Gamma}_{\mathsf{s_y s_z}} = \mathbf{\Gamma}_{\mathsf{s_z s_y}} = \mathbf{0}_{\mathsf{n}\times\mathsf{n}}$ (assuming the vertical dimension is aggregated to a single cell, see Sec. 4.1) and $\mathbf{\Gamma}_{\mathsf{us_z}} = \mathbf{\Gamma}_{\mathsf{s_z u}}^{\mathsf{T}}$ is antisymmetric, due to symmetry in the integrals. Inserting (15) in (8), the augmented solution corresponding to (9) reads then

$$\left[\mathbf{U}^{\mathsf{T}}\ \mathcal{F}\left(\mathsf{s_y}\right)^{\mathsf{T}}\ \mathcal{F}\left(\mathsf{s_z}\right)^{\mathsf{T}}\right]^T = \left(\mathbf{I}_n \otimes \left[\sqrt{\mathsf{S_u}}\mathbf{I}_\mathsf{n}\ \sqrt{\mathsf{S_{s_y}}}\mathbf{I}_\mathsf{n}\ \sqrt{\mathsf{S_{s_z}}}\mathbf{I}_\mathsf{n}\right]\right)\ \left(\mathbf{L} \odot \left(\mathbf{1}_{3\times 3} \otimes \mathbf{\Theta}\right)\right)\ \left[\mathbf{\Phi}_\mathsf{u}\ \ \mathbf{\Phi}_{\mathsf{s_y}}\ \ \mathbf{\Phi}_{\mathsf{s_z}}\right]^T \tag{16}$$

with $\otimes$ the Kronecker product, $\mathbf{1}$ the matrix of ones and the components of the random phase angle vector $\mathbf{\Phi}$ all independent. In practice, correlation of shear components between turbines is small for typical turbine layouts and is of limited value if correlated tangential loads between turbines is not of interest, so $\mathbf{\Gamma}_{\mathsf{s_y s_y}} = \mathbf{\Gamma}_{\mathsf{s_z s_z}} = \mathbf{I}_\mathsf{n}$ and $\mathbf{\Gamma}_{\mathsf{us_z}} = \mathbf{\Gamma}_{\mathsf{s_z u}} = \mathbf{0}_{\mathsf{n}\times\mathsf{n}}$ may be used for simplicity and computational efficiency, yielding *uncorrelated* aggregated shear components for each turbine.

Tangential velocities v and w may also be obtained in a similar way[4]. Although often overlooked, the coherence between u and w is typically nonzero [11]. Coupled generation may then be considered using the same approach as with $\mathsf{s_z}$.

At this point we are able to *theoretically* generate fully correlated timeseries of the linear (axial and tangential) and shear components of the aggregated wind speed vector. The following relates more to practical implementation and multiscale modelling.

[4] Note that IEC standards specify zero coherence in tangential directions, resulting in zero aggregated PSD

3.3 | Constrained turbulence and cascaded construction around turbine points

This section presents a novel solution for constrained turbulence/conditional random process generation using the Moore-Penrose matrix pseudo-inverse, enabling the cascaded, correlated generation of wind speeds at the turbine and farm levels without loss of information.

3.3.1 | Farm domain

As mentioned earlier, the solution is only valid in a stochastic sense and the order at which the different points come may induce unwanted correlation in the realisation, as a property of Cholesky factorisation. It is desirable to treat turbine and grid points separately, first because we may only be interested in turbine points to get power fluctuations, and secondly because measuring wind fluctuations at the turbines is a lot easier than in-between, leading to different validation/calibration approaches. Turbine points may be put first in the Cholesky factorisation –this is the method used in the tool PyConTurb to include user-defined points at the turbine level[24]–, to ensure independence with grid points, but as they are not necessarily located on nodes of a regularly spaced grid, either space interpolation or a non-regularly spaced grid has to be used. While the former brings inaccuracies, the latter is numerically impractical when the number of points becomes large. In addition, solving for grid and turbine points simultaneously raises the question introduced in Sec. 3.1 of which aggregation domain to choose.

The suggested solution that circumvents these issues is to first simulate turbine points, and then construct regular grid points around them in a consistent (read here *coherent*) manner in a second stage.

In the following, only u will be considered for simplicity, extension to other components (v, w, s_y and s_z) being straightforward. Let n_T be the number of turbine points, small in comparison to the number of grid points n_G. In a first stage, the Fourier transform $\mathbf{U}_T$ of u at turbine points is obtained using the method described in the previous sections. Here we are interested in load-equivalent quantities so rotor-based aggregation is used. In a second stage, we are looking for a realisation of the Fourier transform of u at grid points $\mathbf{U}_G$ (this time using cell-based aggregation), that is consistent with the realisation at turbine points, i.e. satisfying

$$\mathbf{P}_T\mathbf{U}_G = \mathbf{U}_T = \sqrt{S_u}\,\mathbf{P}_T\left(\mathbf{L}_G \odot \mathbf{\Theta}_G\right)\widehat{\mathbf{\Phi}}_G = \mathbf{G}_G\widehat{\mathbf{\Phi}}_G$$

with $\mathbf{P}_T$ an $n_T \times n_G$ interpolation matrix mapping grid points to turbine points. This may be achieved by carefully choosing $\widehat{\mathbf{\Phi}}_G$ as

$$\widehat{\mathbf{\Phi}}_G = \mathbf{G}_G^+\mathbf{U}_T + \left(\mathbf{I}_{n_G} - \mathbf{G}_G^+\mathbf{G}_G\right)\mathbf{\Phi}_G = \mathbf{G}_G^+\mathbf{U}_T + \mathbf{G}_G^-\mathbf{\Phi}_G$$

with $\mathbf{G}_G^+$ the $n_G \times n_T$ Moore-Penrose pseudo-inverse[25] of $\mathbf{G}_G$, reading

$$\mathbf{G}_G^+ = \mathbf{G}_G^H\left(\mathbf{G}_G\mathbf{G}_G^H\right)^{-1}$$

$\mathbf{G}_G^- = \mathbf{I}_{n_G} - \mathbf{G}_G^+\mathbf{G}_G$ is the $n_G \times n_G$ nullspace matrix of $\mathbf{G}_G$, and $\mathbf{\Phi}_G$ is an arbitrary vector that we choose so that is satisfies $\left\langle\widehat{\mathbf{\Phi}}_G\widehat{\mathbf{\Phi}}_G^H\right\rangle = \mathbf{I}_{n_G}$ consistently with the random process generation method. It appears that choosing $\mathbf{\Phi}_G$ as a random phase vector as in (9) is a solution, which may be proved using $\left\langle\mathbf{\Phi}_G\mathbf{U}_T^H\right\rangle = \left\langle\mathbf{U}_T\mathbf{\Phi}_G^H\right\rangle^H = \mathbf{0}_{n_G\times n_T}$, $\left\langle\mathbf{\Phi}_G\mathbf{\Phi}_G^H\right\rangle = \mathbf{I}_{n_G}$, $\left\langle\mathbf{U}_T\mathbf{U}_T^H\right\rangle = \mathbf{G}_G\mathbf{G}_G^H$ together with the properties of the pseudo-inverse and nullpsace $\left(\mathbf{G}_G^+\mathbf{G}_G\right)^H = \mathbf{G}_G^+\mathbf{G}_G$; $\mathbf{G}_G\mathbf{G}_G^+ = \mathbf{I}_{n_T}$; $\mathbf{G}_G^-\mathbf{G}_G^{-H} = \mathbf{G}_G^-$, yielding

$$\left\langle\widehat{\mathbf{\Phi}}_G\widehat{\mathbf{\Phi}}_G^H\right\rangle = \mathbf{G}_G^+\left(\left(\mathbf{G}_G\mathbf{G}_G^H\right)\left(\mathbf{G}_G\mathbf{G}_G^H\right)^{-1} - \mathbf{I}_{n_T}\right)\mathbf{G}_G + \mathbf{I}_{n_G} = \mathbf{I}_{n_G}$$

which proves the consistency of the method for providing a *constrained yet random* realisation.

Note 1: Decoupling moduli and arguments not being possible this time, $\mathbf{G}_G$, $\mathbf{G}_G^+$ and $\mathbf{G}_G^-$ are complex-valued.

Note 2: Unlike $\mathbf{\Phi}_G$, $\widehat{\mathbf{\Phi}}_G$ is not necessarily unitary (its components typically have non-unity modulus).

Note 3: $\mathbf{U}_T$ (or parts of) may also be imported from external sources (observed from SCADA data or aggregated from turbine-level turbulence boxes) with appropriate signal processing.

3.3.2 | Turbine domain

Using a similar approach, it is possible to reconstruct a high-resolution turbulence box consistent with the aggregated value $\mathbf{U}_T$ around each turbine. This closes the loop, enabling to get the turbine/minutes and farm/hours scales in an integrated, correlated manner. Let n_H be the number of points in the turbulence box. We are looking for a high-resolution wind field $\mathbf{U}_H$ that relates to $\mathbf{U}_{T_i}$ at turbine point i through weighted integrals (i.e. sums) such as (14), viz.

$$\mathbf{\Psi}\mathbf{U}_H = \mathbf{U}_{T_i} = \sqrt{S_u}\,\mathbf{\Psi}\mathbf{L}_H\widehat{\mathbf{\Phi}}_H = \mathbf{G}_H\widehat{\mathbf{\Phi}}_H$$

with $\boldsymbol{\Psi}$ the weight matrix which may be, if only the u component is simulated at the farm level, $\begin{cases} \boldsymbol{\Psi}_{1i} = 1 & r_0 \leq r \leq R \\ \boldsymbol{\Psi}_{1i} = 0 & r < r_0,\ r > R \end{cases}$; $i = 1 \text{ to } n_H$ with r the radial position of the point and r_0, R the blade root and tip radii respectively. This may straightforwardly be augmented with other components and corresponding weights. The solution is then similar to that of the previous section, viz.

$$\widehat{\boldsymbol{\Phi}}_H = \mathbf{G}_H^+ \mathbf{U}_T + \left(\mathbf{I}_{n_H} - \mathbf{G}_H^+ \mathbf{G}_H\right) \boldsymbol{\Phi}_H;\ \ \mathbf{G}_H^+ = \mathbf{G}_H^T \left(\mathbf{G}_H \mathbf{G}_H^T\right)^{-1};\ \ \boldsymbol{\Phi}_H = \left[e^{i\phi_{H_1}} \cdots e^{i\phi_{H_{n_H}}}\right]^T, \begin{cases} \left\langle \phi_{H_i}, \phi_{H_j} \right\rangle = 1 & i = j \\ \left\langle \phi_{H_i}, \phi_{H_j} \right\rangle = 0 & i \neq j \end{cases}$$

Note that accordingly to the Veers method with frozen-turbulence assumption, $\mathbf{G}_H$ and $\mathbf{G}_H^+$ are real-valued.

4 | IMPLEMENTATION

The method described in the previous sections readily provides as such a mid-fidelity solution to model ambient wind turbulence. However, for practical engineering use, a decent computational time is required. The method suffers from the so-called curse of dimensionality, with computational cost increasing nonlinearly with complexity. Without model order reduction measures, the number of grid points n_G increases proportionally with the farm area. The number of coherence aggregation operations, however, increases with $\mathcal{O}\left(n_G^2\right)$ as does the size of the coherence matrix $\boldsymbol{\Gamma}$, and the cost of the random generation process increases with $\mathcal{O}\left(n_G^3\right)$. Considering a utility-scale farm of 100 turbines with standard spacing and grid resolution (see Sec. 4.1), about 5000 points are needed. The computational time of a 1-hour simulation (to capture farm-scale effects) with standard step size (see Sec. 4.1) on a standard personal computer would be of the order of days. This being deemed incompatible with an engineering solution, efforts have been made to drastically reduce the computational time.

Sec. 4.1 presents how to limit the number of grid points, while Sec. 4.2 aims to decrease the cost of the aggregation operation itself. Finally, Sec. 4.3 presents challenges and solutions related to Cholesky factorisation greatly affecting the computational cost.

4.1 | Farm domain discretisation

The number of points $n_G = n_{G_x} n_{G_y} n_{G_z}$ derives directly from the domain size and grid resolution $\boldsymbol{\Delta}$. The latter should hence be chosen as large as possible, still capturing the relevant physics accurately. The dynamic wake meandering model averages the velocity over the wake diameter in the cross-wind plane[4], so the y and z resolutions should be of comparable size. The definition of wake diameter being unclear in the literature[4], using the rotor diameter D seems a reasonable assumption for $\boldsymbol{\Delta}_z$. As a result, there may only be need for one single aggregated point in the vertical dimension (i.e. $n_{G_z} = 1$) to characterise turbulence[5], and this is assumed in the rest of the paper. This simplifies implementation as the turbulence box is again reduced from 4D to 3D (like for the turbine level, this time not by using the frozen-turbulence assumption to remove x but by using aggregation to remove z). The choice of $\boldsymbol{\Delta}_x$ should be consistent with the distance between two wake planes, i.e. the advection during one time step. This implies choosing a step size Δ_t, which could be based on the largest frequency of significance in aggregated wind speed quantities. However, arguing that aggregation filters out vortices smaller than one rotor diameter suggests the simpler yet pertinent choice of $\boldsymbol{\Delta}_x = D$ and $\Delta_t = \frac{\boldsymbol{\Delta}_x}{u_\infty}$. Finally, $\boldsymbol{\Delta}_y = D$ could also be used, resulting in cubic cells. However, better consistency with the anisotropic nature of coherence (as $\mathbf{a}_x$ is significantly lower than $\mathbf{a}_y$ in (1)[10]) resulting in better numerical consistency and efficiency (see Sec. 4.3.1) suggests using $\boldsymbol{\Delta}_y \approx \frac{\mathbf{a}_x}{\mathbf{a}_y} \boldsymbol{\Delta}_x$.

Assuming ergodicity, the coherence between two points depends only on their *relative* positions. To avoid redundant operations, the aggregated coherence may then be precomputed at regularly-spaced locations covering the entire farm area with a specified grid resolution $\boldsymbol{\Delta}$, resulting in a $n_{G_x} \times n_{G_y}$ look-up table matrix $\boldsymbol{\Sigma}$, thereafter referred to as the kernel matrix (see Sec. 4.3.4). The much larger $n_G \times n_G$ coherence matrix $\boldsymbol{\Gamma}$ is then built using

$$\boldsymbol{\Gamma}_{ij} = \boldsymbol{\Sigma}_{\left\lfloor \frac{j-1}{n_{G_x}} \right\rfloor - \left\lfloor \frac{i-1}{n_{G_x}} \right\rfloor + 1,\ \left(j - n_{G_x} \left\lfloor \frac{j-1}{n_{G_x}} \right\rfloor\right) - \left(i - n_{G_x} \left\lfloor \frac{i-1}{n_{G_x}} \right\rfloor\right) + 1} \tag{17}$$

with $\lfloor\ \rfloor$ the rounding to nearest smaller integer operator.

All frequency components $\mathbf{U}_G$ should be expressed at the same locations (i.e. grid points) prior to inverse Fourier transform. However, if accurate enough, coarser grid resolutions may be used and mapped back to the common specified grid by interpolation. The effective resolution $\widetilde{\boldsymbol{\Delta}}(f)$ and number of points $\widetilde{n}_G(f) = \widetilde{n}_{G_x}(f)\, \widetilde{n}_{G_y}(f)$ may then be adapted to accuracy requirements for each frequency component. An adaption strategy

[5] Note that this is independent to the modelling of the wind profile which may still use high resolution

x_1 \ x_2	$\overline{\psi}_{V_{x_N}}$ u/v/w	$\overline{\psi}_{V_{x_N}}$ $s_{y/z}$	$\overline{\psi}_{V_{x_D}}$ u/v/w	$\overline{\psi}_{V_{x_D}}$ $s_{y/z}$
u/v/w	V_s	$+/-V_s\frac{r_{z/y}}{2}$	V_s	$V_s\left(\frac{\left(\Delta_{z/y}\text{-}\left\|\mathbf{r}_{z/y}\right\|\right)^2+3\mathbf{r}_{z/y}^2}{12}\right)$
$s_{y/z}$	$-/+V_s\frac{r_{z/y}}{2}$	$V_s\left(\frac{\left(\Delta_{z/y}\text{-}\left\|\mathbf{r}_{z/y}\right\|\right)^2-3\mathbf{r}_{z/y}^2}{12}\right)$	$V_s\left(\frac{\left(\Delta_{z/y}\text{-}\left\|\mathbf{r}_{z/y}\right\|\right)^2+3\mathbf{r}_{z/y}^2}{12}\right)$	$V_s\left(\frac{\mathbf{r}_{z/y}^4-\frac{2}{3}\mathbf{r}_{z/y}^2\left(\Delta_{z/y}\text{-}\left\|\mathbf{r}_{z/y}\right\|\right)^2+\frac{1}{5}\left(\Delta_{z/y}\text{-}\left\|\mathbf{r}_{z/y}\right\|\right)^4}{16}\right)$

Table 1 Inner integral of weighting function as function of component, with $V_s=\prod_{\ell=1}^{3}\mathbf{\Delta}_\ell-|\mathbf{r}_\ell|$. Coupling tangential components v, w with shears s_y or s_z is not applicable, nor is coupling s_y with s_z (assuming $n_{G_z}=1$).

based on the rate of change of the kernel matrix is suggested as

$$\widetilde{n}_{G_{x/y}}=\left\lceil\frac{\left\|\delta\mathbf{\Sigma}_{x/y}\right\|}{\epsilon_\gamma}\right\rceil$$

with ϵ_γ a specified tolerance on coherence errors, $\lceil\,\rceil$ the rounding to nearest greater integer operator, and $\delta\mathbf{\Sigma}_{x/y}$ the $(n_{G_x}-1)\times n_{G_y}$ / $n_{G_x}\times\left(n_{G_y}-1\right)$ difference matrices defined as $\delta\mathbf{\Sigma}_{x_{ij}}=\mathbf{\Sigma}_{(i+1)j}-\mathbf{\Sigma}_{ij}$, and $\delta\mathbf{\Sigma}_{y_{ij}}=\mathbf{\Sigma}_{i(j+1)}-\mathbf{\Sigma}_{ij}$. Any matrix norm such as infinite (maximum) or Frobenius (root mean square) may be used. The reduced-order and original coherence matrices $\widetilde{\mathbf{\Gamma}}$ and $\mathbf{\Gamma}$ are then linked through interpolation matrices from full to reduced grid $\mathbf{P}_x(f)$ and $\mathbf{P}_y(f)$ and there reduced-to-full-grid counterparts $\mathbf{P}_x^+(f)$ and $\mathbf{P}_y^+(f)$, both constructed analytically based on weighting of neighbouring points (details are not shown for conciseness):

$$\begin{aligned}\widetilde{\mathbf{\Gamma}}&=\left(\mathbf{P}_x\otimes\mathbf{P}_y\right)\mathbf{\Gamma}\left(\mathbf{P}_x\otimes\mathbf{P}_y\right)^{\mathsf{T}}\\ \mathbf{\Gamma}&\approx\left(\mathbf{P}_x^+\otimes\mathbf{P}_y^+\right)\widetilde{\mathbf{\Gamma}}\left(\mathbf{P}_x^+\otimes\mathbf{P}_y^+\right)^{\mathsf{T}}\end{aligned}$$

Wind velocities are then found using (9) for the reduced grid, and then interpolated back to the original grid, viz.

$$\mathbf{U}\approx\sqrt{S_u}\,\left(\mathbf{P}_x^+\otimes\mathbf{P}_y^+\right)\left(\widetilde{\mathbf{L}}\odot\widetilde{\mathbf{\Theta}}\right)\left(\mathbf{P}_x\otimes\mathbf{P}_y\right)\mathbf{\Phi}\tag{18}$$

4.2 | Aggregation

4.2.1 | Semi-analytical integration

The cell-based sextuple integrals in Sec. 3.1 are excessively costly. Fortunately, through a change of coordinates, the inner integrals may be solved analytically, leaving only a triple integral to be solved numerically. The method is adapted from the derivation of the Mann model[21], noticing that coherence depends only on the relative position between cells through $\overrightarrow{r}_{12}$, not on the individual positions of each cell. Let the elementary integral domain Ω be a volume V representing a cell of dimensions $\mathbf{\Delta}$. Let $\mathbf{r}$ and $\mathbf{s}$ be

$$\mathbf{r}=\vec{r}_{0_2 2}-\vec{r}_{0_1 1};\quad\mathbf{s}=\vec{r}_{0_2 2}+\vec{r}_{0_1 1}$$

Then change variable in (11) and rewrite the integrals over cells as integrals over an infinite volume where parts that lie outside the cell are made zero, viz.

$$\overline{\gamma}_{x_2x_1}=\frac{\int_\infty\int_\infty\gamma_{u_2u_1}\left(\mathbf{p},f,\mathbf{r}+\vec{r}_{0_1 0_2}\right)\,\psi_{V_{x_{1_N}}}\left(\frac{\mathbf{s}-\mathbf{r}}{2}\right)\psi_{V_{x_{2_N}}}\left(\frac{\mathbf{s}+\mathbf{r}}{2}\right)l_1\left(\frac{\mathbf{s}-\mathbf{r}}{2}\right)l_2\left(\frac{\mathbf{s}+\mathbf{r}}{2}\right)|det\left(\mathbf{J}\right)|d\mathbf{r}d\mathbf{s}}{\int_\infty\int_\infty\psi_{V_{x_{1_D}}}\left(\frac{\mathbf{s}-\mathbf{r}}{2}\right)\psi_{V_{x_{2_D}}}\left(\frac{\mathbf{s}+\mathbf{r}}{2}\right)l_1\left(\frac{\mathbf{s}-\mathbf{r}}{2}\right)l_2\left(\frac{\mathbf{s}+\mathbf{r}}{2}\right)|det\left(\mathbf{J}\right)|d\mathbf{r}d\mathbf{s}};\quad\begin{cases}l_k(\mathbf{z})=1 & |\mathbf{z}_i|\le\mathbf{\Delta}_i\\ l_k(\mathbf{z})=0 & |\mathbf{z}_i|>\mathbf{\Delta}_i\end{cases}\quad k=1,2;i=1,2,3;\mathbf{z}\in\mathbb{R}^3\tag{19}$$

with x any of the components u, v, w, s_y, s_z and where subscripts N, D refer to numerator and denominator, respectively. $\mathbf{J}=\frac{\partial\left[\begin{array}{cc}\tilde{\mathbf{r}}_{0_1 1} & \tilde{\mathbf{r}}_{0_2 2}\end{array}\right]^{\mathsf{T}}}{\partial\left[\begin{array}{cc}\mathbf{r} & \mathbf{s}\end{array}\right]^{\mathsf{T}}}$ is the Jacobian between old and new variables, yielding $|\det(\mathbf{J})|=\frac{1}{8}$. Integrating on $\mathbf{s}$ yields

$$\overline{\gamma}_{V_{x_2x_1}}=\frac{\int_{-\mathbf{\Delta}}^{+\mathbf{\Delta}}\gamma_{u_2u_1}\left(\mathbf{p},f,\mathbf{r}+\vec{r}_{0_1 0_2}\right)\overline{\psi}_{V_{x_N}}d\mathbf{r}}{\int_{-\mathbf{\Delta}}^{+\mathbf{\Delta}}\overline{\psi}_{V_{x_D}}d\mathbf{r}}\tag{20}$$

with $\overline{\psi}_V$ analytically integrated weights. Tab. 1 shows $\overline{\psi}_V$ for the various velocity components assuming unitary weighting from wind speed to aerodynamic loads and omitting the wind profile as a first step.

Note that the denominator in (19) and (20) may be integrated fully analytically, without need for coordinate change. However, for numerical accuracy it is desirable that discretisation errors are present in both numerator and denominator and semi-analytical integration should be applied to both.

Wind profile

The weighting function representing the wind profile will likely be too complex for semi-analytical integration, even the simple power law showing no practical analytical solution. In the context of turbulence aggregation, however, a linear approximation around turbine hub height (z origin) seems reasonable:

$$u\left(z\right) \approx u\left(0\right)\left(1 + k\frac{z}{\mathbf{\Delta}_z}\right)$$

with k a linear coefficient that may in its simplest form[6] be taken as

$$k = \frac{\mathbf{\Delta}_z}{u_\infty}\left.\frac{du}{dz}\right|_{z=0}$$

i.e. the gradient of the total wind speed at z = 0 and u = 0. In its linearised form, the wind profile's weighting function becomes similar to that of the vertical shear s_y. The integrated weights accounting for wind profile $\widehat{\overline{\psi}}_V$ that involve component u, v or w (s_y and s_z are independent on the wind profile) are then obtained by combination with the s_y entry in Tab. 1. For instance for $x_1 = x_2 =$ u , numerator:

$$\widehat{\overline{\psi}}_{V_{uu_N}} = \overline{\psi}_{V_{uu_N}} + \frac{k}{\mathbf{\Delta}_z}\overline{\psi}_{V_{us_{yN}}} + \frac{k}{\mathbf{\Delta}_z}\overline{\psi}_{V_{s_yu_N}} + \left(\frac{k}{\mathbf{\Delta}_z}\right)^2\overline{\psi}_{V_{s_ys_{yN}}} = V_s\left(1 + \left(\frac{k}{\mathbf{\Delta}_z}\right)^2\frac{\left(\mathbf{\Delta}_z\text{-}|\mathbf{r}_z|\right)^2 - 3\mathbf{r}_z^2}{12}\right)$$

Rotor-based averaging

A similar method may be used to reduce rotor-based quadruple integrals on a disc A in polar coordinates. In this case $\mathbf{r} = \rho_\mathbf{r}\left[\begin{array}{ccc} 0 & \cos\theta_\mathbf{r} & \sin\theta_\mathbf{r}\end{array}\right]^\mathsf{T}$, $\mathbf{s} = \rho_\mathbf{s}\left[\begin{array}{ccc} 0 & \cos\theta_\mathbf{s} & \sin\theta_\mathbf{s}\end{array}\right]^\mathsf{T}$, and

$$\overline{\gamma}_{A_{x_2x_1}} = \frac{\int_0^{2\pi}\int_0^{2R}\gamma_{u_2u_1}\left(\mathbf{p}, f, \mathbf{r} + \vec{r}_{0_10_2}\right)\overline{\psi}_{A_{x_N}}\rho_\mathbf{r}d\rho_\mathbf{r}d\theta_\mathbf{r}}{\int_0^{2\pi}\int_0^{2R}\overline{\psi}_{A_{x_D}}\rho_\mathbf{r}d\rho_\mathbf{r}d\theta_\mathbf{r}};\ \ \overline{\psi}_{A_{x_X}} = \int_0^{2\pi}\int_0^{\rho_{\mathbf{s}_{max}}}\psi_{A_{x_1X}}\left(\frac{\mathbf{s}-\mathbf{r}}{2}\right)\psi_{A_{x_2X}}\left(\frac{\mathbf{s}+\mathbf{r}}{2}\right)\rho_\mathbf{s}d\rho_\mathbf{s}d\theta_\mathbf{s} \tag{21}$$

with R the disc (i.e. rotor) radius, X = N or D and $\rho_{\mathbf{s}_{\mathsf{max}}}$ the upper bound for radial integration on $\mathbf{s}$ yielding

$$\rho_{\mathbf{s}_{max}} = \sqrt{4 - \rho_\mathbf{r}^2\sin^2\left(\theta_\mathbf{r} - \theta_\mathbf{s}\right)} - \rho_\mathbf{r}\left|\cos\left(\theta_\mathbf{r} - \theta_\mathbf{s}\right)\right|$$

In practice only the innermost integral in (21) (i.e. radial in $\mathbf{s}$) may admit an analytical solution, provided that the weighting function is analytical and simple enough. Computational benefit may therefore only be seen when the number of averaging points becomes large. An alternative may be to integrate over a disc only for the more important PSD calculations (i.e. elements 1 and 2 are one and the same), and else over a square as an approximation (equivalent to a 2D reduction of cell-based averaging and hence only a double integral). An other alternative used in [7] is to keep the original coordinates but assume $\gamma_{u_2u_1}$ is only dependent on the difference between azimuthal angles, again allowing to solve for one inner integral analytically.

4.2.2 | Numerical integration

The remainder of the integral is computed numerically through discretisation with a sufficient number of points, which may be chosen in an adaptive manner based on the tolerance ϵ_γ. One single point will typically be sufficient for low frequencies and large distances, Sørensen even assumed that turbine-to-turbine aggregated coherence was equal to point-based. For short distances (neighbouring grid points) and mid frequencies, however, the nonlinearity of coherence leads to significant errors when approximated to the integral domain's centre value, and hence requires a finer mesh. At high frequencies, coherence between points may be neglected.

4.3 | Nearest correlation matrix

Random process generation using Cholesky factorisation as presented in Sec. 2.2 is ill-defined if the coherence matrix $\mathbf{\Gamma}$ (or its reduced-order version $\widetilde{\mathbf{\Gamma}}$) is not positive-definite (abbreviated p.-d.). This appears to be an issue for dense farm-level coherence matrices (both point-based and aggregated, see Sec. 4.3.3), and may be a —if not The— major driver for computational cost. Two approaches may be considered to ensure p.-d.ness:

[6] Better approximations minimising the space- and/or time-average of the absolute or squared error may also be devised

- Top-down approach: non-intrusive, optimal in terms of induced errors, but not scalable; presented in Sec. 4.3.1
- Bottom-up approach: intrusive (model-dependent), suboptimal, but scalable; presented in Sec. 4.3.3

4.3.1 | The alternate projection algorithm

Finding the nearest p.-d. matrix is a common problem when working with real data. The Nearest Correlation Matrix (NCM) algorithm was suggested by Higham[26] based on the alternate projection method of Dykstra[27]. It is based on artificially forcing p.-d.ness by replacing the negative eigenvalues of the matrix by slightly positive ones (in the following, uniformly equal to λ_+) through a projection onto the p.-d. space P_{PD} involving the eigenvalue-eigenvector decomposition. This alters the matrix' diagonal, which is then forced to unity in a second stage through another projection P_{U}. Doing so creates negative eigenvalues which should then be replaced by positive ones, and so on. After $\mathsf{n}_{\mathrm{NCM}}$ iterations and starting with $\widehat{\mathbf{\Gamma}}_0 = \widetilde{\mathbf{\Gamma}}$ and $\mathbf{\Delta}\widehat{\mathbf{\Gamma}}_{\mathrm{PD}_0} = \mathbf{0}_{\mathsf{n}_\mathsf{G}\times\mathsf{n}_\mathsf{G}}$, the algorithm reads:

$$\begin{cases} \widehat{\mathbf{\Gamma}}_{2\mathsf{n}_{\mathrm{NCM}}+1} & = \mathsf{P}_{\mathrm{PD}}\left\{\widehat{\mathbf{\Gamma}}_{2\mathsf{n}_{\mathrm{NCM}}} - \mathbf{\Delta}\widehat{\mathbf{\Gamma}}_{\mathrm{PD}_{\mathsf{n}_{\mathrm{NCM}}-1}}\right\} = \mathbf{V}\mathbf{\Lambda}_+\mathbf{V}^{\mathsf{T}} + \lambda_+\mathbf{I}_{\mathsf{n}_\mathsf{G}};\ \widehat{\mathbf{\Gamma}}_{2\mathsf{n}_{\mathrm{NCM}}} - \mathbf{\Delta}\widehat{\mathbf{\Gamma}}_{\mathrm{PD}_{\mathsf{n}_{\mathrm{NCM}}-1}} - \lambda_+\mathbf{I}_{\mathsf{n}_\mathsf{G}} = \mathbf{V}\mathbf{\Lambda}\mathbf{V}^{\mathsf{T}};\ \mathbf{\Lambda}_{+_{\mathsf{ii}}} = \max\left(\mathbf{\Lambda}_{\mathsf{ii}}, 0\right), \mathsf{i}=1\text{ to }\mathsf{n}_\mathsf{G} \\ \mathbf{\Delta}\widehat{\mathbf{\Gamma}}_{\mathrm{PD}_{\mathsf{n}_{\mathrm{NCM}}}} & = \mathsf{P}_{\mathrm{PD}}\left\{\widehat{\mathbf{\Gamma}}_{2\mathsf{n}_{\mathrm{NCM}}+1} - \mathbf{\Delta}\widehat{\mathbf{\Gamma}}_{\mathrm{PD}_{\mathsf{n}_{\mathrm{NCM}}-1}}\right\} - \widehat{\mathbf{\Gamma}}_{2\mathsf{n}_{\mathrm{NCM}}+1} + \mathbf{\Delta}\widehat{\mathbf{\Gamma}}_{\mathrm{PD}_{\mathsf{n}_{\mathrm{NCM}}-1}} \\ \widehat{\mathbf{\Gamma}}_{2\mathsf{n}_{\mathrm{NCM}}+2} & = \mathsf{P}_{\mathrm{U}}\left\{\widehat{\mathbf{\Gamma}}_{2\mathsf{n}_{\mathrm{NCM}}+1}\right\} = \widehat{\mathbf{\Gamma}}_{2\mathsf{n}_{\mathrm{NCM}}+1} - \mathrm{Diag}\left(\widehat{\mathbf{\Gamma}}_{2\mathsf{n}_{\mathrm{NCM}}+1}\right) + \mathbf{I}_{\mathsf{n}_\mathsf{G}} \end{cases} \tag{22}$$

with $\widehat{\mathbf{\Gamma}}_{2\mathsf{n}_{\mathrm{NCM}}}$ the current NCM candidate and $\mathbf{\Delta}\widehat{\mathbf{\Gamma}}_{\mathrm{PD}_{\mathsf{n}_{\mathrm{NCM}}}}$ the Dykstra correction providing integral action ensuring convergence toward a p.-d. matrix that minimises the error with the original matrix in the least-square (Frobenius norm) sense[26].

Each iteration involves a full eigen decomposition, whose cost is, although also $\mathcal{O}\left(\mathsf{n}_\mathsf{G}^3\right)$, at least one order of magnitude higher than Cholesky factorisation. Keeping $\mathbf{\Gamma}$ p.-d. for as many frequency components as possible is then crucial to reduce the overall cost. A first measure is to choose $\mathbf{\Delta}$ so that it decays evenly in x and y directions, hence the suggestion in Sec. 4.1. In practice, experience shows that a couple of iterations is sufficient, and the maximum (infinite norm) error is seldom higher than ϵ_γ.

The NCM algorithm is also a major driver for memory usage, as several temporary matrices of order n_G need to be stored simultaneously.

4.3.2 | Shrinking cross components

A cheaper but less accurate approach when one has a reference p.-d. matrix to start with is shrinking[28]. This may be used for the arguably less important cross blocks $\mathbf{\Gamma}_{\mathsf{us}_\mathsf{z}}$ and $\mathbf{\Gamma}_{\mathsf{uw}}$, where the diagonal blocks are attributed higher priority and made p.-d. beforehand (using the top-down approach of Sec. 4.3.1 or the bottom-up approach of Sec. 4.3.3). The block-diagonal matrix with cross blocks removed becomes p.-d., and may be used as a basis for shrinking, which consists in finding the smallest value α such that

$$\widehat{\mathbf{\Gamma}} = \begin{bmatrix} \widehat{\mathbf{\Gamma}}_{\mathsf{uu}} & \mathbf{0}_{\mathsf{n}_\mathsf{G}\times\mathsf{n}_\mathsf{G}} & (1-\alpha)\,\mathbf{\Gamma}_{\mathsf{s}_\mathsf{z}\mathsf{u}} \\ \mathbf{0}_{\mathsf{n}_\mathsf{G}\times\mathsf{n}_\mathsf{G}} & \widehat{\mathbf{\Gamma}}_{\mathsf{s}_\mathsf{y}\mathsf{s}_\mathsf{y}} & \mathbf{0}_{\mathsf{n}_\mathsf{G}\times\mathsf{n}_\mathsf{G}} \\ (1-\alpha)\,\mathbf{\Gamma}_{\mathsf{us}_\mathsf{z}} & \mathbf{0}_{\mathsf{n}_\mathsf{G}\times\mathsf{n}_\mathsf{G}} & \widehat{\mathbf{\Gamma}}_{\mathsf{s}_\mathsf{z}\mathsf{s}_\mathsf{z}} \end{bmatrix};\ 1 \geq \alpha \geq 0$$

is p.-d. (here $\mathsf{u}, \mathsf{s}_\mathsf{y}, \mathsf{s}_\mathsf{z}$ are used as example components). This may be solved using a bisection algorithm.

4.3.3 | Shrinking anisotropy of farm-level coherence

The alternate projections algorithm is appropriate for the first stage of Sec. 3.3.1 which involves only turbine points and hence relatively small matrices with higher need for minimising errors. For the second stage involving many more points and only affecting wake dynamics, it is desirable to trade accuracy for computational efficiency. This section presents a bottom-up alternative, starting from the point-based coherence model and using the analogy with Gaussian process models[29] where a kernel is used to generate the covariance matrix of a given quantity evaluated/measured at different points. In our case, $\mathbf{\Sigma}$ introduced in Sec. 4.1 may be seen as the kernel matrix of aggregated turbulence, used to generate the coherence matrix $\mathbf{\Gamma}$, directly related to the covariance matrix used in Gaussian process models through integration over frequency.

Take u as an example (straightforwardly extendable to v and w, setting aside shear components as they only are relevant at turbine points). Kernel theory tells that $\mathbf{\Gamma}_{\mathsf{uu}}$ is p.-d. whenever $\mathbf{\Sigma}_{\mathsf{uu}}$ is p.-d., which is in turn granted if the generating function (13) of $\mathbf{\Sigma}_{\mathsf{uu}}$ is itself p.-d.. For point-based coherence as used in turbine-level turbulence box modelling, this amounts to (1) p.-d.. For aggregated coherence, it is trivial to show that p.-d.ness is preserved in the aggregation process, as the latter is merely a combination of sum of p.-d. kernels, translation of p.-d. kernels and multiplication by positive constants (best seen using the semi-analytically integrated form of the aggregated coherence in (21)) which all preserve p.-d.ness[30]. This is however valid only if the same number of averaging points is used for all kernel entries.

As a consequence, p.-d.ness of the aggregated coherence matrix is granted whenever the point-based coherence function belongs to or is constructed from well-known p.-d. kernel families, with two particularly relevant families in our case:

- Completely monotone radial basis functions[31] of the form $\gamma = \mathrm{f}\left(\left\|\overrightarrow{\mathrm{r}}_{12}\right\|^2\right)$ with $(-1)^{\mathrm{n}} \frac{\mathrm{d}^{\mathrm{n}}\mathrm{f}}{\mathrm{d}\left\|\overrightarrow{\mathrm{r}}_{12}\right\|^{\mathrm{n}}} > 0 \; \forall \mathrm{n} \in \mathbb{N}$, i.e. the kernel is only dependent on the norm of the position vector (i.e. distance) squared $\left\|\overrightarrow{\mathrm{r}}_{12}\right\|^2$ and the corresponding derivatives are positive for any differentiation order. This occurs when $\mathbf{a}$ and $\mathbf{b}$ are isotropic and positive ($\mathbf{a} = \mathrm{a}\left(\left\|\overrightarrow{\mathrm{r}}_{12}\right\|\right)[111]^{\mathsf{T}}$, $\mathbf{b} = \mathrm{b}\left(\left\|\overrightarrow{\mathrm{r}}_{12}\right\|\right)[111]^{\mathsf{T}}$, $\mathrm{a}, \mathrm{b} \in \mathbb{R}^+$) but not necessarily independent on $\left\|\overrightarrow{\mathrm{r}}_{12}\right\|$.
- Anisotropic powered exponential kernels of the form $\gamma = \mathrm{e}^{-\left\|\mathbf{a}\otimes\overrightarrow{\mathrm{r}}_{12}\right\|\frac{\mathrm{f}}{\mathrm{u}_\infty}}$. This occurs when $\mathbf{b} = \mathbf{0}_{3\times1}$ and all components of $\mathbf{a}$ are positive and independent on the position vector, but not necessarily isotropic.

While turbine-level coherence models have been built with p.-d.ness in mind and belong to one of these categories (typically the first one), Sørensen's model described by (2) falls in between the two and its p.-d.ness is hence not guaranteed, although close. The bottom-up approach to the NCM problem consists then in bringing the coherence function closer to one of the two p.-d. kernel families, thus guaranteeing p.-d.ness in an intrusive manner but with little computational effort.

Keeping in mind that this is only actual for the second stage mostly important for wake meandering and that longitudinal coherence has been found not to affect meandering to a large extent[6], choice is made to preserve the lateral decay factor and hence rather shrink toward the first of the above-introduced kernels by modifying the longitudinal decay factor, viz.

$$\widetilde{a_{long}} = \alpha\, a_{long} + (1-\alpha)\, a_{lat}$$

with $0 \leq \alpha \leq 1$ the shrinking coefficient with an initial value of 1.

4.3.4 | Kernel pre-generation

Independently on the approach, it is possible to pre-generate p.-d. aggregated coherence kernels for a specific wind condition/spectral model in a first simulation, to speed up later computations. p.-d. matrices may then be directly generated for other random variable realisations (i.e. seeds, enabling efficient generation of samples for e.g. Monte Carlo simulations), turbine layouts, grid sizes (provided the precomputed kernel covers the entire farm area) or time discretisations and durations (provided the precomputed kernel matches frequency components). Using the bottom-up approach, this is straightforwardly done by aggregating the shrinked point-based kernel of Sec. 4.3.3. The top-down approach implies further considerations presented in the following.

With (17) describing its generation process from $\mathbf{\Sigma}_{\mathrm{uu}}$, $\mathbf{\Gamma}_{\mathrm{uu}}$ is a block-Toeplitz matrix whose blocks are themselves Toeplitz –i.e. a *Toeplitz-block-Toeplitz* matrix– reading

$$\mathbf{\Gamma}_{uu} = \begin{bmatrix} \mathbf{\Gamma}_{\mathrm{uu}_{\mathrm{x}_0}} & \mathbf{\Gamma}^{\mathsf{T}}_{\mathrm{uu}_{\mathrm{x}_1}} & \cdots & \mathbf{\Gamma}^{\mathsf{T}}_{\mathrm{uu}_{\mathrm{x}_{\mathrm{n}_{\mathrm{G_x}}}}} \\ \mathbf{\Gamma}_{\mathrm{uu}_{\mathrm{x}_1}} & \mathbf{\Gamma}_{\mathrm{uu}_{\mathrm{x}_0}} & \ddots & \vdots \\ \vdots & \ddots & \ddots & \mathbf{\Gamma}^{\mathsf{T}}_{\mathrm{uu}_{\mathrm{x}_1}} \\ \mathbf{\Gamma}_{\mathrm{uu}_{\mathrm{x}_{\mathrm{n}_{\mathrm{G_x}}}}} & \cdots & \mathbf{\Gamma}_{\mathrm{uu}_{\mathrm{x}_1}} & \mathbf{\Gamma}_{\mathrm{uu}_{\mathrm{x}_0}} \end{bmatrix}, \quad \mathbf{\Gamma}_{\mathrm{uu}_{\mathrm{x}_\mathrm{i}}} = \begin{bmatrix} \mathbf{\Sigma}_{\mathrm{uu}_{\mathrm{i}1}} & \mathbf{\Sigma}_{\mathrm{uu}_{\mathrm{i}1}} & \cdots & \mathbf{\Sigma}_{\mathrm{uu}_{\mathrm{i}_{\mathrm{n}_{\mathrm{G_y}}}}} \\ \mathbf{\Sigma}_{\mathrm{uu}_{\mathrm{i}2}} & \mathbf{\Sigma}_{\mathrm{uu}_{\mathrm{i}1}} & \ddots & \vdots \\ \vdots & \ddots & \ddots & \mathbf{\Sigma}_{\mathrm{uu}_{\mathrm{i}2}} \\ \mathbf{\Sigma}_{\mathrm{uu}_{\mathrm{i}_{\mathrm{n}_{\mathrm{G_y}}}}} & \cdots & \mathbf{\Sigma}_{\mathrm{uu}_{\mathrm{i}2}} & \mathbf{\Sigma}_{\mathrm{uu}_{\mathrm{i}1}} \end{bmatrix} \tag{23}$$

where grid points are listed in column-major order. Hence, inversely, the nearest p.-d. kernel $\widehat{\mathbf{\Sigma}}_{\mathrm{uu}}$ may be retrieved from the *nearest positive-definite Toeplitz-block-Toeplitz unit-diagonal* matrix of $\mathbf{\Gamma}_{\mathrm{uu}}$. This implies adding into the alternate projection algorithm a projection $\mathrm{P}_{\mathrm{TBT}}$ onto the Toeplitz-block-Toeplitz space, which is simply an averaging of diagonals (adapted from Grigoriadis et al.[32]):

$$P_{TBT}\left\{\mathbf{\Sigma}_{uu}\right\}_{ij} = \frac{1}{\left(n_{G_x}-i+1\right)\left(n_{G_y}-j+1\right)} \sum_{k=1}^{n_{G_x}-i+1} \sum_{\ell=1}^{n_{G_y}-j+1} \widehat{\mathbf{\Gamma}}_{uu_{(i+k-2)n_{G_y}+j+\ell-1,\,(k-1)n_{G_y}+\ell}}$$

where indexing of $\widehat{\mathbf{\Gamma}}$ refers to matrix elements and not iterations. Follows a reconstruction of $\widehat{\mathbf{\Gamma}}_{\mathrm{uu}}$ using (17) or (23). Although overlooked by Grigoriadis et al. in their paper, it can be shown that $\mathrm{P}_{\mathrm{TBT}}$ does not need to be attributed a Dykstra correction[27] –like P_{U}, but unlike P_{PD}–, as it is linear (the projection of a sum equals the sum of projections of its elements).

5 | NUMERICAL EXPERIMENTS

The goal of this section is to illustrate turbulence aggregation and the associated concepts and methods presented in this paper. It shows the consistency and efficiency of the approach in a qualitative manner, detailed validation against higher-fidelity farm simulations and measurements being more related to calibration and left as further work.

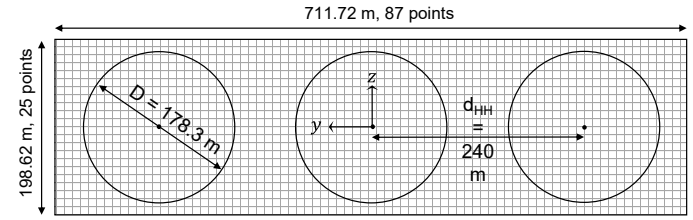

Figure 1 Domain used for verification against point-based Gaussian process synthetic turbulence generation

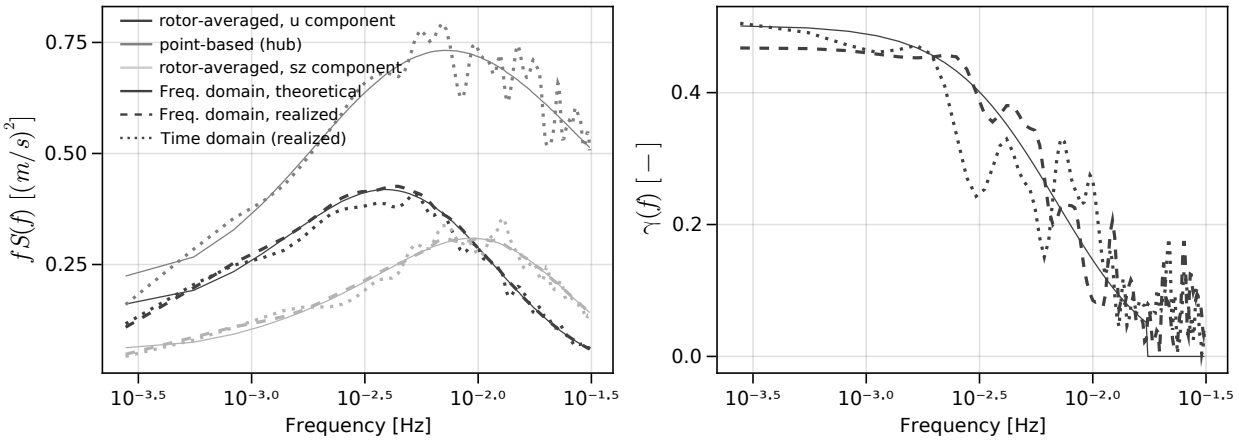

Figure 2 Spectrum and coherence, point-based versus aggregated and desired versus realised (seed-averaged)

5.1 | Turbine scale

In order to validate the aggregation concept, comparison with turbine-scale simulations has been performed through an academic case study. The domain is as illustrated in Fig. 1:

- on the one hand three adjacent (closely-spaced) turbine points simulated using the model presented in this paper
- on the other hand a point-based turbulence box covering the same area, simulated in NREL's TurbSim synthetic turbulence simulation code used a reference. Aggregation -i.e. space averaging- is then performed in the time domain over each of the three virtual rotor areas.

The Kaimal spectrum and corresponding coherence model defined by IEC standard 61400-1 ed.3 with turbulence class B have been used in the two simulations, for a wind speed of 10 m/s, and the DTU 10MW [33] reference wind turbine rotor to define hub height and rotor area for averaging. No farm-level turbulence model has been used (this will result in somewhat lower correlation between rotors). 10 seeds of each simulation are considered, and mean spectral quantities (PSD and coherence) over all seeds are looked at for comparison, in addition to theoretical aggregated values as defined by (11) to (13). The left-hand side of Fig. 2 shows PSDs of point-based and aggregated u and s_z components, while the right-hand side shows the coherence between two adjacent rotors.

Fig. 3 illustrates the concept of turbulence box reconstruction from aggregated values, using a modified version of NREL's TurbSim able to sync aggregated values over multiple adjacent rotors. The left-hand plots shows timeseries of aggregated values for the parent (aggregated solution) and child (point-based reconstruction). The small discrepancy there may be attributed to discretisation errors, resolution being rather coarse to cope with the large domain while maintaining computational efficiency. The right-hand plot shows the PSD of a rotationally-sampled wind field, averaging over the blades with a weighting function proportional to radial location (consistently with actuator-disc aggregation in polar coordinates as done by Sørensen et al. [7]) and taking rotor speed as constant. The good match between regular (fully random) and synced turbulence box generation shows the ability of the latter to consistently reconstruct high-resolution wind fields while matching pre-defined aggregated values, and generally speaking the soundness of the suggested method for constrained synthetic turbulence generation.

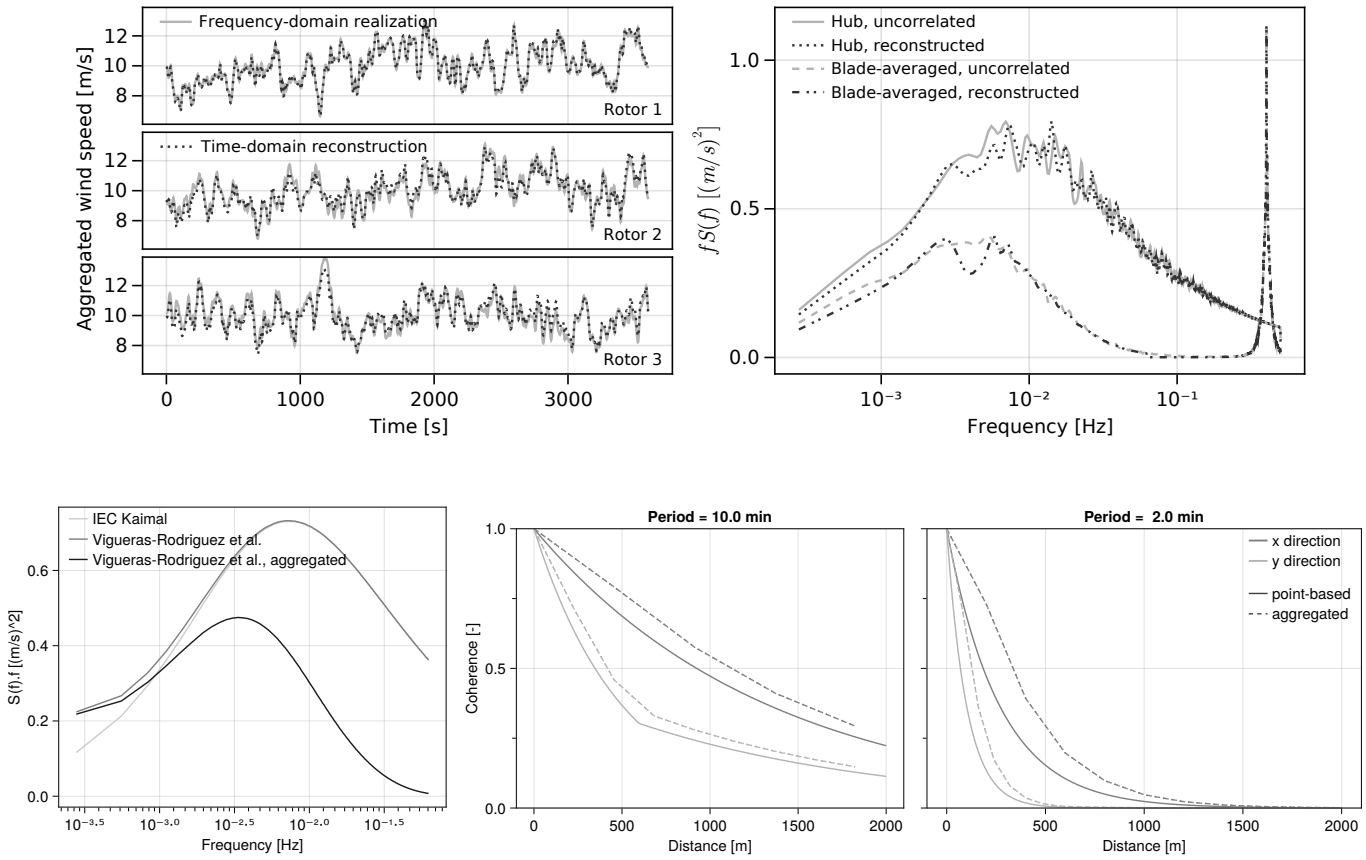

Figure 4 Wind spectrum and coherence

5.2 | Farm scale

A case study is performed on the TotalControl reference wind power plant [34] with 32 DTU 10MW turbines placed in a staggered pattern, in the same wind conditions as in Sec. 5.1. The farm-scale spectral model of Vigueras-Rodriguez et al. [9,10] with original parameters is chosen here for its simplicity and validation against power measurements from multiple Danish offshore wind farms. Multiple 1-h realisations are generated, playing with a selection of parameters for illustration of the model's capabilities regarding power fluctuations (turbine points) and wake meandering (grid points).

5.2.1 | Aggregated coherence

The left-hand side plot of Fig. 4 shows the low-pass filtering effect of aggregation on the wind spectrum and the additional low-frequency content suggested by [9]. The centre and right-hand side plots show the effect of aggregating coherence versus the original point-based model of [10]. This effect increases significantly with frequency. When considering only turbine points as done by Sørensen et al., i.e. distances above five diameters – in the current case about 1km –, approximating aggregated coherence to point-based may be reasonable. For grid points however, aggregated values should be used – though the impact of inaccuracies on top of the existing uncertainty on wake dynamics may be questioned (see Sec. 5.2.3).

5.2.2 | Power fluctuations

The power is modelled using a simplistic representation of the wind turbine controller and a power coefficient:

$$P = min\left(C_{p_{max}}\frac{1}{2}\rho A\left(U_{mean}+u\right)^3, P_{rtd}\right)$$

with P_{rtd} the rated power and $C_{P_{max}}$ the maximum power coefficient. Contributions from individual turbine are then summed up and normalised by installed capacity before computing PSD and averaging over realisations. The left-hand side of Fig. 5 shows the effect of farm-scale modelling

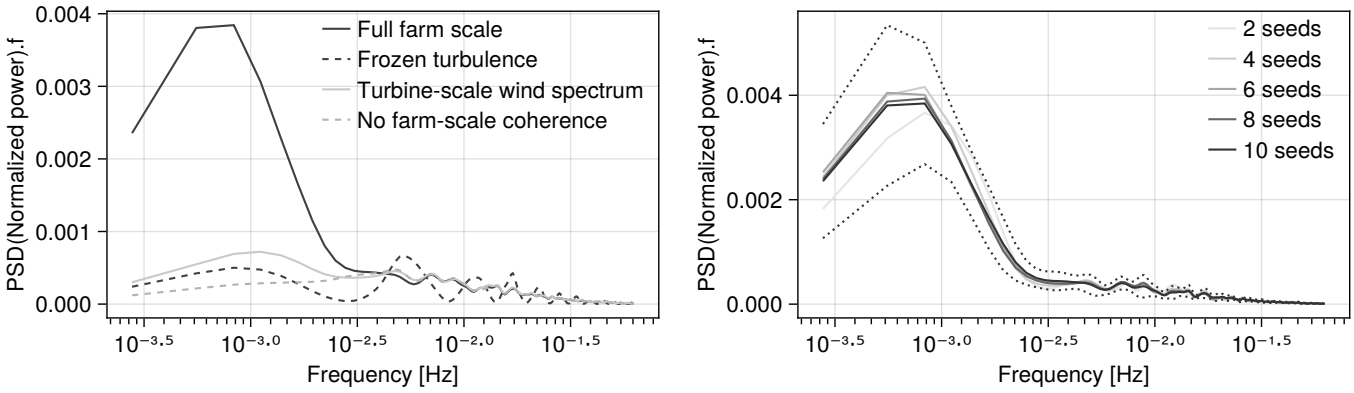

Figure 5 Power fluctuations

features –farm-scale wind spectrum, farm-scale coherence function[7] and frozen-turbulence assumption. It is seen that missing any of the farm-scale features leads to underestimation of low-frequency fluctuations (periods larger than five minutes). Perhaps even more interesting are the frequency-domain oscillations observed when using the frozen-turbulence assumption, which are actually as expected since the simplistic time-delay correlation leads to fluctuations between up- and downwind turbines being more or less in phase depending on frequency. At this stage, a conclusion would be that as far as power fluctuations are concerned, it is better not to use any coherence model than the frozen-turbulence assumption.

The right-hand side of Fig. 5 aims at showing the importance of running Monte Carlo simulations based on multiple stochastic realisations, just like turbine-level analyses use multiple 10-min high-resolution realisations. The dotted line in the figure correspond to $\pm$ the standard deviations over 10 realisations, representing the uncertainty of studies based on a single simulation.

5.2.3 | Wake meandering

While the frozen-turbulence assumption has been deemed valid for the modelling of wake meandering by Shaler et al.[6], significant differences were observed in wake meandering pathlines when compared to LES and were found heavily dependent on the calibration process. While this is still hypothetical at this stage and remains to be proven, lifting the frozen-turbulence assumption by use of aggregated synthetic turbulence generation is believed to provide a more solid representation closer to physics and hence with a lesser need for calibration and filtering. Fig. 6 shows alongwind spatial variations of the lateral wind speed in the wake of turbine 1, obtained by taking values along a line parallel to the X axis for a particular realisation. Fig. 7 shows pathlines in the XY plane of parcels entering the domain for three realisations, computed using a simple transport equation in Lagrangian coordinates similar to that used for wake meandering. The starting point coincides with the domain's upwind boundary and phase angles are identical between cases, so they all share the same initial conditions. As expected from Fig. 6, frozen turbulence removes a large part of wind fluctuations so the pathlines show less amplitude and are smoother. Not using farm scale-specific models for the wind spectrum and coherence function also yields differences from the fully coherent farm-scale baseline, which relate more to model calibration, while the significantly different trends obtained with the frozen-turbulence assumption put its validity into question.

5.2.4 | Efficiency

The effects on total computational time of generating multiple stochastic realisations and of farm size –considering a farm of four times the size in terms of area with 128 turbines– are shown in Tab.2. The baseline generates one single seed for the above-described case study. Note that CPU time is larger than real time, as the calculation is partly multi-threaded on a machine with multiple cores. The curse of dimensionality is clearly observed, multiplying CPU time by about 13 times for a 4 times larger farm. This non-linear increase occurs in the coherence matrix building and decomposition phase, which is common to all realisations. Therefore, the computational speed decreases increases less than linearly with the number of seeds, and the relative effect of the latter becomes smaller as farm size increases.

Fig.8 shows the effect of the NCM algorithm and tolerance (ϵ_γ in Sec. 4.1 and 4.2.2, also used to defined convergence criteria in 4.3) on the processing of the coherence matrix (NCM algorithm + Cholesky decomposition) for the first frequency components. Decreasing tolerance in the

[7] using standard turbine-scale coherence models at farm scale yields in practice zero coherence between turbines due to the large decay factor

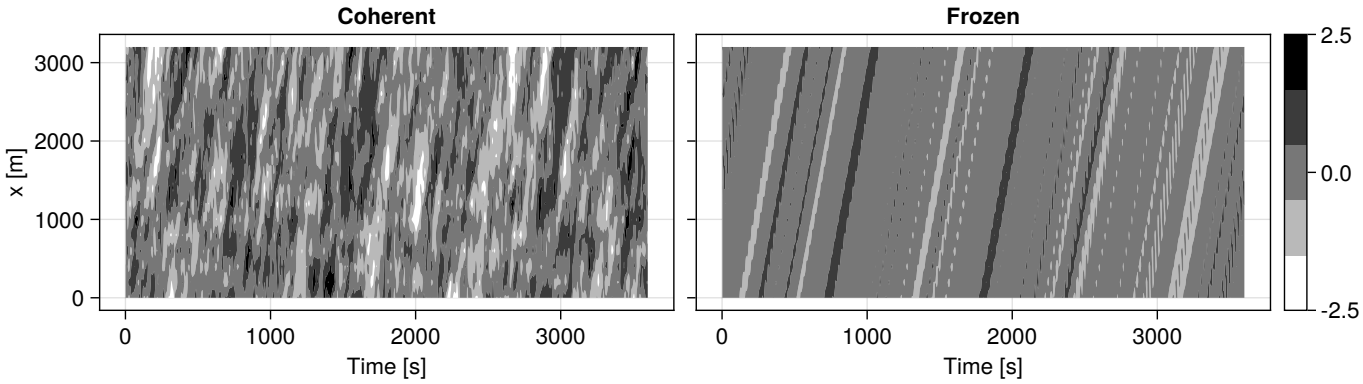

Figure 6 Slice along X axis (Y=0) of a sample aggregated wind field realisation, lateral component

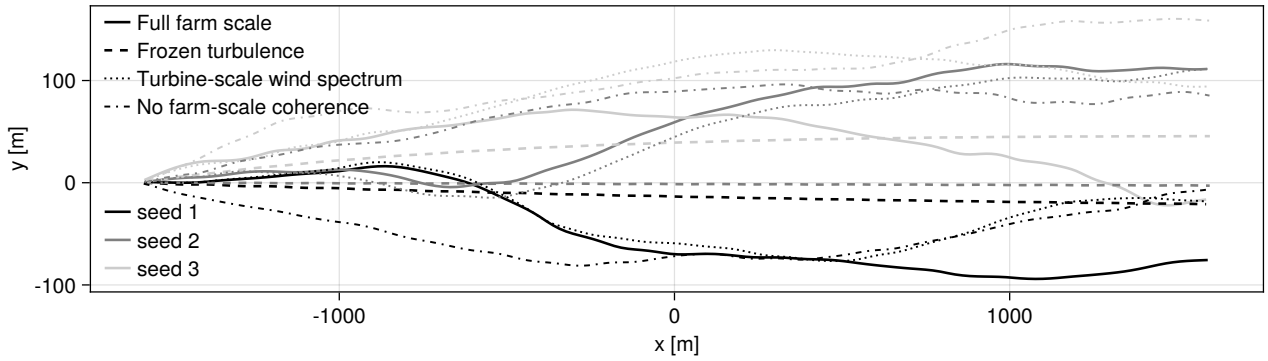

Figure 7 Samples of horizontal meandering pathlines

Baseline	10 seeds	Large farm
1407	5744	18343

Table 2 Total CPU time [seconds]

128-turbine farm yields denser adaptive grids enabling illustrating the effect of grid size. While top-down NCM is slightly faster for smaller matrices (as it does not imply re-aggregating coherence), its efficiency becomes critically poor as the number of points increases. Looking at the maximum error (infinite norm of the difference between the original non-positive-definite matrix and the NCM), the top-down NCM algorithm yields values two order of magnitudes lower than its bottom-up counterpart. Although the maximum error induced by the bottom-up algorithm may seem large (up to 0.25), the effect on results is better represented through the average weighted absolute error defined as $\frac{\sum\sum\left|\gamma_{original}-\gamma_{NCM}\right|\gamma_{original}}{n_G^2}$, which is about 5 times smaller.

6 | CONCLUSION

A method for farm-wide, correlated synthetic turbulence generation based on Gaussian process generation has been suggested. It is based on the concept of aggregated turbulence and more specifically aggregated coherence, which characterises large turbulent vortices responsible for global wind turbines loads, wake dynamics and farm-wide power fluctuations. The method consists in averaging coherence in space in the frequency domain prior to Gaussian process generation (i.e. translating to time domain through inverse Fourier transform). This enables to drastically reduce the number of degrees of freedom and hence, among others, to lift the frozen-turbulence assumption used in point-based representations. Major improvements to the original method suggested by P. Sørensen's research group at Risø/DTU are (1) the modelling of turbulence not only at but also between turbines, as input to farm simulation codes using the dynamic wake meandering model, and (2) the reconstruction of turbine-scale

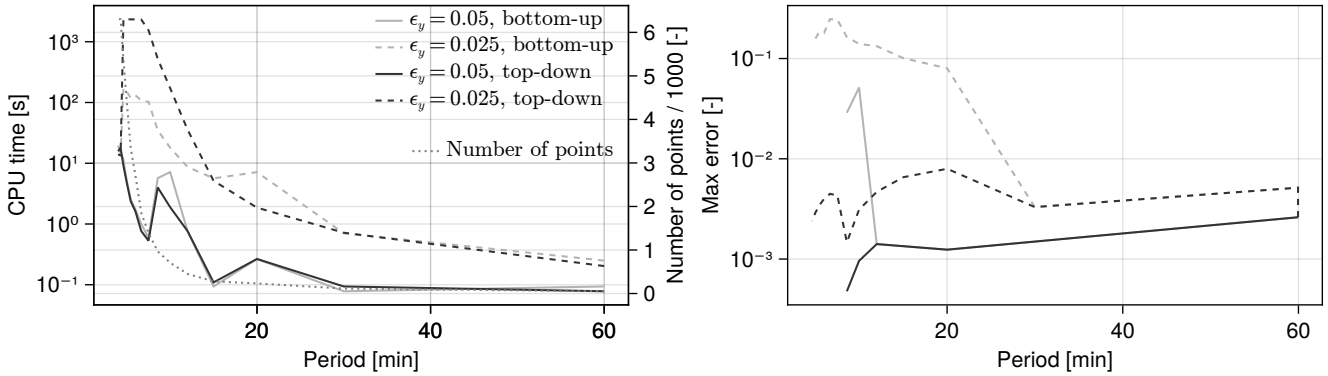

Figure 8 CPU times, grid size and NCM-induced error as function of tolerance and NCM algorithm

point-based (opposite to aggregated) high-resolution wind fields in a correlated manner. Key enabling mathematical subtleties for practical implementation are thoroughly presented. The model has been verified against a state-of-the-art point-based counterpart at small scale. Its superiority for the modelling of power fluctuations and potentially wake dynamics in large wind farms is then illustrated.

This paper focuses on the theoretical background behind the method rather than on its use and validation. More work is needed to validate the methods against measurements of power fluctuations from recent large wind farms, updating the work of Sørensen et al.. Deeper understanding and validation should also be obtained by comparison with LES simulations and hindcast weather data. This will require a calibration of underlying spectral models and a tuning of parameters such as grid resolution.

ACKNOWLEDGEMENTS

NREL is gratefully acknowledged for the open-source development of the FAST ecosystem for which –among other uses– the present method is designed, and on which it is based in its implementation. This work has been financed by the European Commission through the WATEREYE project (grant nr. 851207) and the Research Council of Norway through the CONWIND project (grant nr. 304229) and FME NorthWind research centre (grant nr. 321954).

References

1. Veers P, Dykes K, Lantz E, et al. Grand challenges in the science of wind energy. *Science* 2019; 366(6464).

2. Madsen HA, Larsen GC, Larsen TJ, Troldborg N, Mikkelsen R. Calibration and validation of the dynamic wake meandering model for implementation in an aeroelastic code. *Journal of Solar Energy Engineering* 2010; 132(4).

3. IEC 61400-3-1 . Wind energy generation systems - Part 3-1: Design requirements for fixed offshore wind turbines. *International Electrotechnical Commission, Geneva* 2019.

4. Jonkman J, Shaler K. Fast. farm user's guide and theory manual. 2018; National Renewable Energy Laboratory Golden, CO.

5. OpenFAST. https://github.com/OpenFAST/openfast; .

6. Shaler K, Jonkman J, Doubrawa Moreira P, Hamilton N. FAST. Farm response to varying wind inflow techniques. tech. rep., National Renewable Energy Lab.(NREL), Golden, CO (United States); Boulder, CO (USA): 2019.

7. Sørensen P, Hansen AD, Rosas PAC. Wind models for simulation of power fluctuations from wind farms. *Journal of wind engineering and industrial aerodynamics* 2002; 90(12-15): 1381–1402.

8. Sørensen P, Cutululis NA, Vigueras-Rodríguez A, et al. Modelling of power fluctuations from large offshore wind farms. *Wind Energy: An International Journal for Progress and Applications in Wind Power Conversion Technology* 2008; 11(1): 29–43.

9. Vigueras-Rodríguez A, Sørensen P, Cutululis NA, Viedma A, Donovan M. Wind model for low frequency power fluctuations in offshore wind farms. *Wind Energy* 2010; 13(5): 471–482.

10. Vigueras-Rodríguez A, Sørensen P, Viedma A, Donovan MH, Lázaro EG. Spectral coherence model for power fluctuations in a wind farm. *Journal of Wind Engineering and Industrial Aerodynamics* 2012; 102: 14–21.

11. Cheynet E, Jakobsen JB, Reuder J. Velocity spectra and coherence estimates in the marine atmospheric boundary layer. *Boundary-layer meteorology* 2018; 169(3): 429–460.

12. Burton T, Jenkins N, Sharpe D, Bossanyi E. *Wind energy handbook*. Wiley . 2013.

13. Shinozuka M, Jan CM. Digital simulation of random processes and its applications. *Journal of sound and vibration* 1972; 25(1): 111–128.

14. Huang G, Liao H, Li M. New formulation of Cholesky decomposition and applications in stochastic simulation. *Probabilistic Engineering Mechanics* 2013; 34: 40–47.

15. Veers PS. Three-dimensional wind simulation. tech. rep., Sandia National Labs.; Albuquerque, NM (USA): 1988.

16. Apt J. The spectrum of power from wind turbines. *Journal of Power Sources* 2007; 169(2): 369–374.

17. Larsén XG, Vincent C, Larsen S. Spectral structure of mesoscale winds over the water. *Quarterly Journal of the Royal Meteorological Society* 2013; 139(672): 685–700.

18. Larsén XG, Larsen SE, Petersen EL, Mikkelsen TK. A Model for the Spectrum of the Lateral Velocity Component from Mesoscale to Microscale and Its Application to Wind-Direction Variation. *Boundary-Layer Meteorology* 2021; 178(3): 415–434.

19. Göçmen T, Larsén XG, Imberger M. The effects of open cellular convection on wind farm operation and wakes. In: . 1618. IOP Publishing. ; 2020: 062014.

20. Jonkman BJ. TurbSim user's guide: Version 1.50. 2009.

21. Mann J. Wind field simulation. *Probabilistic engineering mechanics* 1998; 13(4): 269–282.

22. Bachynski EE, Chabaud V, Sauder T. Real-time Hybrid Model Testing of Floating Wind Turbines: Sensitivity to Limited Actuation. *Energy Procedia* 2015; 80: 2–12. doi: 10.1016/j.egypro.2015.11.400

23. Chabaud V. Rotor-integrated modeling of wind turbine aerodynamics. *Wind Energy* 2021.

24. Rinker JM. PyConTurb: an open-source constrained turbulence generator. In: . 1037. IOP Publishing. ; 2018: 062032.

25. Petersen KB, Pedersen MS. The matrix cookbook. 2012.

26. Higham NJ. Computing the nearest correlation matrix: a problem from finance. *IMA journal of Numerical Analysis* 2002; 22(3): 329–343.

27. Boyle JP, Dykstra RL. A method for finding projections onto the intersection of convex sets in Hilbert spaces. In: Springer. 1986 (pp. 28–47).

28. Higham NJ, Strabic N, Sego V. Restoring definiteness via shrinking, with an application to correlation matrices with a fixed block. *SIAM Review* 2016; 58(2): 245–263.

29. Williams CK, Rasmussen CE. Gaussian processes for regression. 1996.

30. Fasshauer GE. Positive definite kernels: past, present and future. *Dolomites Research Notes on Approximation* 2011; 4: 21–63.

31. Schoenberg IJ. Metric spaces and completely monotone functions. *Annals of Mathematics* 1938: 811–841.

32. Grigoriadis KM, Frazho AE, Skelton RE. Application of alternating convex projection methods for computation of positive Toeplitz matrices. *IEEE transactions on signal processing* 1994; 42(7): 1873–1875.

33. Bak C, Zahle F, Bitsche R, et al. The DTU 10-MW reference wind turbine. *Danish wind power research 2013* 2013.

34. Andresen S, Madariaga A, Merz K, Meyers J, Munters W, Rodriguez C. Reference Wind Power Plant. *TotalControl Deliverable D1.3* 2018.